Journal of Materials Chemistry A

# Conductivity of Cold Sintered Diphasic Composites Containing a Ceramic Active Material and a Solid-State Electrolyte or Carbon for All Solid-State Batteries

| | |
|---|---|
| Journal: | *Journal of Materials Chemistry A* |
| Manuscript ID | TA-ART-11-2023-007067.R1 |
| Article Type: | Paper |
| Date Submitted by the Author: | 15-Jan-2024 |
| Complete List of Authors: | Grady, Zane; Pennsylvania State University, Materials Science and Engineering; Materials Research Institute<br>Fan, Zhongming; Penn State - Main Campus, Materials Science and Engineering<br>Fanghanel, Julian; Pennsylvania State University<br>Randall, Clive; Pennsylvania State University, Center for Dielectric Studies, Materials Research Institute, University Park, Pa 16802 USA, |
| | |

# Conductivity of Cold Sintered Diphasic Composites Containing a Ceramic Active Material and a Solid-State Electrolyte or Carbon for All Solid-State Batteries

Zane M. Grady*[1,2], Zhongming Fan[1,2], Julian Fanghanel[1,2], Clive A. Randall*[1,2]

[1]*Department of Materials Science and Engineering, The Pennsylvania State University, University Park, PA, United States, 16802*

[2]*Materials Research Institute, The Pennsylvania State University, University Park, PA, United States, 16802*

***Corresponding authors**

*Email: zane.grady@pnnl.gov (Z. Grady), car4@psu.edu (C.A. Randall)*

## 1. Abstract

For solid-state batteries based on ceramic materials, the means of effective materials processing and co-processing presents a significant challenge. The high sintering temperature required for many solid electrolytes induces alkali volatilization, in addition to preventing the co-procesing with other battery materials, such as carbon or active materials. In this paper, we demonstrate how cold sintering, a low temperature sintering process driven by chemomechanical pressure-solution creep in the presence of a transient solvent and uniaxial pressure, can fabricate dense ceramic matrix composites containing an electroactive material with either carbon or a ceramic solid electrolyte with minimal loss of phase/function. The model system is composed of the $Na_3V_2(PO_4)_3$ (NVP) active material, the $Na_3Zr_2Si_2PO_{12}$ (NZSP) solid electrolyte, and carbon black/carbon nanofibers.

The conductivity of the carbon-NVP composites is fitted to a classical percolation model, demonstrating low percolation thresholds (2-4 vol.%). By measuring the electrical properties of a range of composite compositions, a more complete view of mixed conduction phenomena through the diphasic composites is obtained. In contrast, impedance spectroscopy measurements of diphasic composites containing active material and solid electrolyte (NVP and NZSP, respectively) reveals a gradual transition to fast ionic conduction as the composition ranges from pure active material to primarily solid electrolyte dominated (vol.% NZSP > 90%). These results may also be useful in future studies which require a detailed understanding of conductivity as a function of composition in order to optimize for electrochemical properties such as volumetric energy density or rate performance.

**Keywords:** solid-state batteries, solid electrolytes, composites, mixed conduction, impedance spectroscopy, cold sintering, ceramic processing,

## 2. Introduction

Lithium-ion batteries have formed the basis for numerous industries, such as the matured consumer electronics industry and the nascent electric vehicle market. Until this point, the properties and economics of these incumbent lithium-ion based technologies, with liquid electrolytes and carbonaceous anodes, have proved sufficient for the rapid growth of certain industries such as consumer electronics and electric vehicles. For these industries to improve further, and for new energy storage industries to be established, new types of rechargeable batteries will need to be developed.[1]

Sodium-ion batteries have been proposed as an alternative to the incumbent lithium-ion technology.[2] Sodium is a much more naturally abundant element meaning that batteries based on sodium have the potential to be less expensive and be less subject to supply chain disruptions compared to lithium. However, the higher redox potential of sodium metal (-2.71 versus SHE, 0.34 V higher than Li), larger ionic radius, and lower energy density of sodium compared to lithium means that, in general, the performance of sodium-ion batteries falls well-short of state-of-the-art lithium-based benchmarks.[3] Thus, the cost benefits afforded by sodium must be weighed against the diminished electrochemical performance in order to make a compelling argument for the technology.[3,4]

In order to maximize the energy density of sodium-ion batteries, the use of a metallic sodium anode and a high voltage cathode is required. Sodium metal anodes are quite prone to dendrite growth[5] and thus a solid electrolyte will likely be required. Thus, sodium solid-state batteries (NaSSBs), characterized by a solid electrolyte and ideally a Na-metal anode, are a promising articulation of sodium-based technologies. However, many prior works have shown that the fabrication of solid-state batteries which are simultaneously thin, of low resistance, mechanically robust, and inexpensive is very difficult[6–9].

Solid-state batteries can be categorized into distinct types based on the kind of solid electrolyte employed (polymer, glass, ceramic, composites, etc.) and/or method of manufacturing (cold pressing, hot pressing, casting from solution, thin film sputtering, etc.). Comprehensive comparisons from different perspectives have been given elsewhere in the literature.[1,8,10–12] Pertinent to this work is the generally agreed upon conclusion that ceramic oxide solid electrolytes demonstrate excellent thermal, mechanical, and chemical stability, but the high temperature sintering process required to turn powders into dense ceramics prohibits their widespread adoption in solid-state batteries.[9,13] The high temperature ceramic sintering process usually requires temperatures in the range of 800°C to 1200°C in order to remove porosity and form well-bonded grain boundaries, but these temperatures are incompatible with co-processing coherent interfaces between the solid electrolyte and solid electrodes or forming homogenous composites of the solid electrolyte with the active materials and conductive additives (e.g. layered oxides and carbon, respectively).[9,13–16]

In light of these apparent thermal processing incompatibilities, a number of means of solid-state battery fabrication have been proposed. Most commonly, a polymer or gel solid electrolyte is used to form a continuous framework for ion transport within and between the two electrodes.[17–21] The fabrication of these batteries is relatively simple given the ductile nature of polymer solid electrolytes, but the thermal/mechanical stability, ionic conductivity, and transference number of these materials are generally poor.[22,23] An alternative route is the use of soft inorganic solid electrolyte materials, such as glasses based on the Li-P-S ternary system[24,25], which allow for the fabrication of multilayered[26,27] and composite electrodes[28–33] at low temperatures/pressures. These glassy materials, however, often suffer from ambient atmosphere instability and a limited electrochemical stability window.[34] To employ ceramic solid electrolytes while avoiding co-processing, some researchers have demonstrated the ability to form a partially porous scaffold of solid electrolyte, into which the active material can be infiltrated into after the ceramic scaffold is sufficiently sintered.[6,35–44] Monolithic solid-state batteries have also been formed using various sputtering techniques, but these are limited by cost, total capacity, and ability to co-sputter different materials/composites.[45–53] Finally, it is possible to modify the sintering conditions (temperature, pressure, time, presence of a sintering aid) to induce densification at more benign conditions relative to the conventional sintering process. This category includes the application of liquid phase sintering, field-assisted sintering, hot pressing to solid-state battery manufacturing.[8,11,41,54–

[65] Our previous work[66–69] has applied a relatively new sintering technique termed “cold sintering”[70–73] to the fabrication of solid-state sodium-ion batteries. The cold sintering process has certain advantages over the other aforementioned modified sintering techniques which this work seeks to demonstrate and quantify.

The cold sintering process is characterized by the use of driving forces (temperature, pressure, chemical potential) for sintering applied to a particulate compact in an open system.[70,74,75] In practice, this is accomplished by mixing the powder to be sintered (a ceramic solid electrolyte) with a “transient solvent” (e.g. water or a low temperature salt), which is loaded into a uniaxial die heated while under pressure. The applied temperature need only be above the melting/boiling point of the transient solvent (typically 100°C to 400°C), whereupon the solvent at the particle-particle contact points drives a dissolution-precipitation diffusional process, resulting in sintering of the powder while simultaneously driving the solvent out of the densifying system. This process appears similar to the geological pressure-solution creep process[70], and has been shown to be effective in promoting low temperature densification of a wide range of ceramics and metals. It is important to note that cold sintering is generally one of, if not the, lowest temperature processing technique capable of producing dense ceramics (compared to liquid phase and field-assisted sintering techniques), which makes it an attractive means of producing composites/multilayered systems of ceramics with more thermally fragile materials, as is desirable for solid-state batteries.

We have recently shown that the cold sintering process can be applied to the $Na_3V_2(PO_4)_3$ (NVP, active material)-$Na_3Zr_2Si_2PO_{12}$(NZSP, solid electrolyte)-carbon system to form dense monolithic composites of high electronic/ionic conductivity while retaining electrochemical activity.[67] In this work, it was shown that by diphasic composites of NVP with either carbon or NZSP exhibited apparently enhanced electronic or ionic conductivity, respectively. The present work seeks to more closely examine this by systematically varying the composite of these binary composites to unveil underlying trends in these changes to the magnitude and nature of the bulk conductivity of the diphasic composites. As outlined in the preceding paragraphs, solid-state batteries are certain to be composite in nature, (e.g., having dense, mixed conducting electrodes) so it will be necessary to understand how the conductivities of the individual materials, such as the ionic conductivity of the solid electrolyte and the electronic conductivity of the carbon, augment the intrinsic conductivity of the active material (here, NVP) to result in sufficient bulk electronic and ionic conductivities to drive the redox reaction. Further, it is desirable to minimize the volume of conductive agents needed in the composite electrodes to maximize energy density. This has been explored for conventional liquid electrolyte-based batteries[76] but has not yet been studied extensively for sintered ceramic solid-state batteries given the difficulties in forming dense composites without degradation.[60] It should be noted that recent studies have however applied a similar approach to exploring the relationship between bulk conductivity and composite electrode composition for soft (plastically deformable) inorganic solid electrolyte systems.[77,78] To this end, most of the findings of this work should be generally applicable to solid-state battery composite electrodes formed by means other than the cold sintering process and utilizing other inorganic polycrystalline solid electrolytes.

This paper first describes the process of cold sintering diphasic composites of our model system (NVP-NZSP-carbon) and probes the crystal structures of the densified composites as well as their microstructure to demonstrate the absence of degradation. This advantage of cold sintering is emphasized by measuring onset of thermal decomposition of the diphasic composites, illustrating that solid-state batteries based on these materials should be fabricated below 600°C. Then, impedance measurements are taken for numerous series of composites containing increasing amounts of carbon (either spherical or of high-aspect-ratio in morphology) or NZSP solid electrolyte. The resulting impedance spectra and apparent bulk conductivity are coupled with microstructural observations to begin to elucidate the processing-composition-property relationships as it pertains to polycrystalline solid-state battery materials. Finally, these results are contextualized broadly for their potential contributions to practical solid-state battery design beyond the considered model system.

## 3. Experimental

### Materials

The $Na_3V_2(PO_4)_3$ (NVP, $\rho$ = 3.16 g.cm$^{-3}$) and $Na_3Zr_2Si_2PO_{12}$ (NZSP, $\rho$ = 3.26 g.cm$^{-3}$) powders were synthesized *via* a sol-gel process as described in our previous works[67,68]. The only modification for this study was the use of a 5% $H_2$ 95% Ar (vol.%) atmosphere to carry out the NVP calcination to ensure a reducing atmosphere. The carbon black was purchased from MTI (Super P, $\rho$ = 1.6 g.cm$^{-3}$). The carbon nanofibers were purchased from US Research Nanomaterials

Inc. (unfunctionalized, no dispersant, $\rho$ = 2.1 g.cm$^{-3}$). The NaOH transient solvent was purchased from Sigma Aldrich and stored in a glovebox or under vacuum until cold sintering.

## Mixing of Powders

Three types of diphasic powder mixtures were investigated: (1) NZSP + NVP, (2) NVP + carbon black, and (3) NVP + carbon nanofibers. In each case, the appropriate amount of the pure powder was weighed and charged into a 25 mL glass vial. A single yttria-stabilized zirconia ball (Ø = 5 mm) was added to the unmixed powders and the vial was sealed and placed inside a planetary centrifugal mixer (Thinky Mixer Model no. ARE-250). The mixture was then mixed for one minute followed by a manual re-agitation to break up any agglomerates formed, with this process repeated ten times.

## Cold Sintering

The 10 wt.% (~14 vol.%) of solid NaOH ($T_m$ = 312 °C) was then added to the so-mixed diphasic powder mixtures and mixed by hand in a mortar and pestle, briefly and in a fume hood to avoid carbonate formation. The NaOH-diphasic powder mixture was then added to a stainless-steel die (Across International, Ø = 13 mm) with nickel foil spacers (0.1 mm thick, Alfa Aesar 99%) and fitted with a mica band heater. The die and heater where then placed into a standard Carver press and simultaneously heated to 375°C and pressed uniaxially at 350 MPa. The platens of the press were heated to 340°C to reduce thermal loss to the environment. These conditions were held for three hours, at which point the pressure was released and the die cooled with a 6-inch fan. The dense cold sintered pellet was then extracted and stored under vacuum for further characterization. A schematic representation of the mixing of the powders with subsequent cold sintering is shown in **Scheme 1**.

## Characterization

X-ray diffraction (XRD) was carried out on both the powders and the surfaces of the cold sintered pellets using a PANalytical Empyrean diffractometer in Bragg-Brentano configuration using Cu, K$\alpha$ radiation. All scans were carried out in a 2Θ range of 5-70° with a tension of 45 kV, current of 40 mA, a step size of 0.01°, and a dwell time of 200 sec.step$^{-1}$. Both fracture surfaces and polished surfaces of the cold sintered pellets were sputtered with an iridium characterized using scanning electron microscopy (SEM) utilizing a Verios Field Emission NanoSEM equipped with an EDS system. The TEM specimens were prepared by Focused Ion Beam (Scios 2, FEI). To prevent any sodium loss due to local heating, the entire FIB process was conducted at the liquid nitrogen temperature. The prepared specimen was subsequently loaded to a cryogenic TEM holder. The TEM (Talos X, FEI) was operated at 200 kV at the liquid nitrogen temperature too, for the sake of potential beam damage. The EDS mapping was collected by the Super-X EDS detector. The density of the pellets was measured using Archimedes method with ethanol as the liquid medium.

To characterize the samples using electrochemical impedance spectroscopy (EIS), the surfaces of the pellets were first polished to 2400 grit and 100 nm platinum electrodes were applied using magnetron sputtering (Quorum Technologies, EMS-150R-S). The EIS measurements were then taken using a two-probe electrode fixture connected to an impedance spectrometer (Modulab XM MTS). The EIS measurements were taken from 1 MHz to 0.05 Hz with a 10 mV ac bias relative to 0 V dc unless otherwise noted. For EIS measurements at elevated temperatures, the fixture was placed in a Delta Design Oven (model no. 9023) which was heated to the desired temperature and let equilibrate for 5 minutes prior to measurement. The impedance data was fit using the Zview software package (Scribner Associates).

Thermogravimetric analysis (TGA) and differential scanning calorimetry (DSC) was performed using a thermal analyzer (Netzsch STA 449 F3 Jupiter®). The measurements were performed in air between 20 °C and 1200 °C with a heating rate of 10 °C/min.

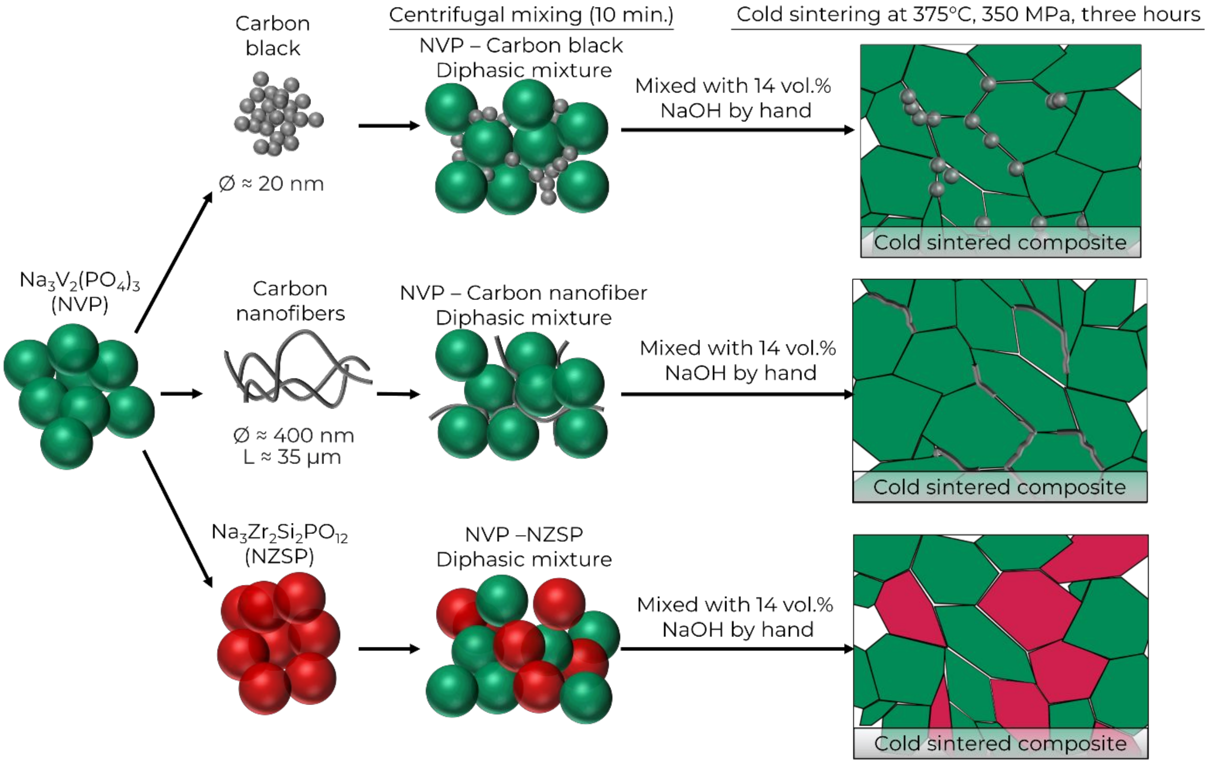

***Scheme 1*** *A schematic of the materials processing employed in work. First, three diphasic powder mixtures (NVP + carbon black, NVP + carbon nanofibers, and NVP + NZSP) are weighed in varying volume fractions and mixed centrifugally. These mixtures are then mixed with NaOH and cold sintered, resulting in dense diphasic ceramic matrix pellets.*

## 4. Phase purity and microstructure of diphasic composites

The aim of this section is to demonstrate the retention of phase purity in the cold sintered composites and that the microstructure of the composites contains the desired features of the composites, namely the distribution of carbon at the grain boundaries of a sintered ceramic and distinct grains of active material adjacent to solid electrolyte grains. To emphasize the benefits of the low-temperature cold sintering method in producing these composites, this section also demonstrates the approximate thermal processing limitations of the model system by observing the onset of thermal degradation.

## 4.1 Cold sintering enables retention of primary phases in dense ceramic composites

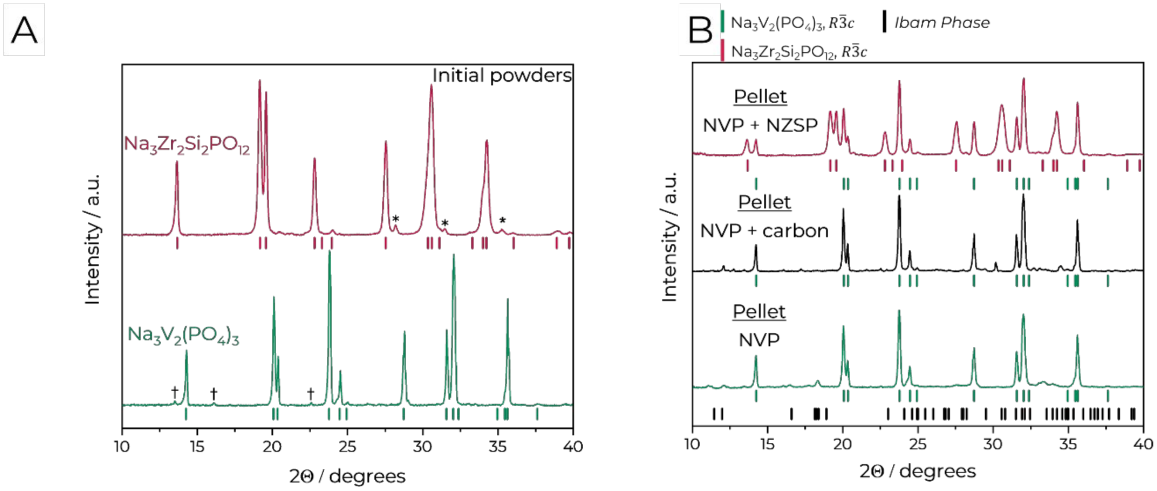

***Figure 1*** *The XRD pattern of the as-synthesized ceramic powders is shown in (**A**). The XRD patterns of the pure NVP, a diphasic composite containing carbon fibers+NVP, and a diphasic composite containing NZSP+NVP are shown in (**B**). PDF for reference structures, NVP phase: 00-062-0345*[79]*, $Na(VO)_2(PO_4)_2{\cdot}4H_2O$ phase: 04-010-9272, NZSP phase: 04-017-0758*[80]*, Ibam (no. 72) phase: 01-076-4696*[81]*.*

The X-ray diffraction (XRD) patterns of the active material, $Na_3V_2(PO_4)_3$ (henceforth abbreviated NVP), and the solid-state electrolyte, $Na_3Zr_2Si_2PO_{12}$ (henceforth abbreviated NZSP), powders are presented in **Figure 1A**. These two materials share the general "NASICON" crystallographic structure, with both phases being indexed to $R\bar{3}c$ symmetry (space group: 167)[80]. By noting the 2Θ peak locations for the major reflections of each material, we find that the NVP powder has lattice parameters of $a = b = 8.72$ Å and $c = 21.81$ Å, while the NZSP powder has lattice parameters of $a = b = 9.07$ Å and $c = 22.91$ Å. The NZSP powder has a small $ZrO_2$ impurity, denoted by (*) which is commonly observed as a synthesis byproduct. The NVP powder has a few minor peaks not indexed to the primary NASICON phase († in **Figure 1A**) which is attributed to a sub-oxide hydrate ($Na(VO)_2(PO_4)_2{\cdot}4H_2O$) of the main phase. The NVP powder was then mixed with either a prescribed volume of the NZSP powder, or carbon (carbon black or nanofibers), and cold sintered. The cold sintering parameters were identified in our prior work, namely the addition of 10 wt.% (14 vol.%) of NaOH to the powder mixture, followed by simultaneous heating and pressing at 375°C and 350 MPa, respectively, for three hours. These conditions were found to optimal for high density, phase pure, pellets relative, which is described in previous papers.[67,68]

The XRD spectra of three cold sintered pellets containing (1) 100 vol.% NVP ceramic, (2) 92.5 vol.% NVP with 5.8 vol.% carbon nanofiber and (3) 60 vol.% NVP and 40 vol.% NZSP, is shown in **Figure 1B**. The XRD pattern of cold sintered pure NVP can be indexed to the same NASICON structure as the initial powder, with no observed changes in the lattice parameters relative to the powder. Additionally, a small low symmetry secondary phase is apparent in the spectra after cold sintering, having *Ibam* symmetry (space group: 72) similar to a number of low symmetry sodium-vanadium-phosphate compounds identified by previous studies[81,82]. These phases often have mixed vanadium oxidation states, which might be caused here by some partial vanadium oxidation during cold sintering. Other than the presence of this secondary phase, the cold sintered NVP, the cold sintered composites containing both carbon and NZSP retain the primary crystal structures of interest, as shown in **Figure 1B**. It is also worth noting that, in the composite samples containing NVP and NZSP, there are no major shifts in lattice parameters ($\Delta < 0.15\%$) for either the NVP or the NZSP phase, indicating that there is no major inter-diffusion of sodium or other metals between the distinct phases during cold sintering.

## 4.2 Demonstration of thermal limitation to co-processing the composite materials

It is difficult to produce dense diphasic ceramic-matrix composites of these materials using conventional ceramic processing techniques, such as high temperature sintering. This is because the high temperatures required for sintering are usually around $^2/_3$ of the melting temperature (~1200°C for NZSP) which induces degradation of more thermally fragile materials, such as the NVP, or undesired chemical interaction between the distinct phases of the composite. To emphasize this point, and demonstrate how cold sintering addresses the issue, we attempted to estimate the maximum temperature at which the materials of interest (NVP, NZSP, and carbon) could be co-processed without degradation or interaction. Similar to prior work[9,13], we demonstrate this by heating materials either individually or as diphasic mixed powders in a TGA/DSC apparatus under air to correlate changes in mass/heat flux with degradation as a function of temperature (**Figure 2**).

When the NZSP solid electrolyte powder is heated under air by itself, it shows no degradation (i.e., mass loss) until 1200°C (**Figure 2A**), which was chosen as the upper temperature limit as this is near the typical sintering temperature for polycrystalline NZSP ceramics.[83] In contrast, the pure carbon and NVP active material undergo significant decomposition (i.e., weight change) around 640°C (**Figure 2A**).

The diphasic mixtures of NVP-carbon and NVP-NZSP also exhibit either weight loss (indicating gaseous decomposition) or weight gain (potentially indicating oxidation) around the same temperature (ca. 600°C), as also shown in **Figure 2A**. This is further illustrated by examining diphasic powder mixtures heated in a tube furnace to representative temperatures, which are then subsequently examined using XRD (**Figure 2B**). **Figure 2B** magnifies a 2Θ range where characteristic peaks for the NVP and NZSP phase are present, which allows for clear correlation between the heating temperature and changes in the material structure. By this simple method, we can show that simply heating a diphasic mixture of NVP and NZSP powders to 510°C in a tube furnace results in complete loss of the two characteristic peaks of the NVP phase (**Figure 2B**, left panel). Heating to higher temperatures (637°C and 790°C) results in both the loss of the NZSP peaks and the appearance of new secondary phase peaks.

Diphasic mixtures of carbon fibers and NVP decompose at similar temperatures (**Figure 4B**, right panel). All peaks corresponding to the parent NVP phase are lost by 510°C. Attempting to heat the mixture to higher temperatures results in the complete loss of the sample due to melting (**Figure S1**). These decomposition events can be avoided by reducing the processing temperature to 375°C using cold sintering, resulting in composites which retain the primary peaks of the ceramic phases after densification (**Figure 1B** and **Figure 2B**). These experiments emphasize the importance of low temperature processing methods, such as cold sintering, in enabling solid-state batteries based on composites.

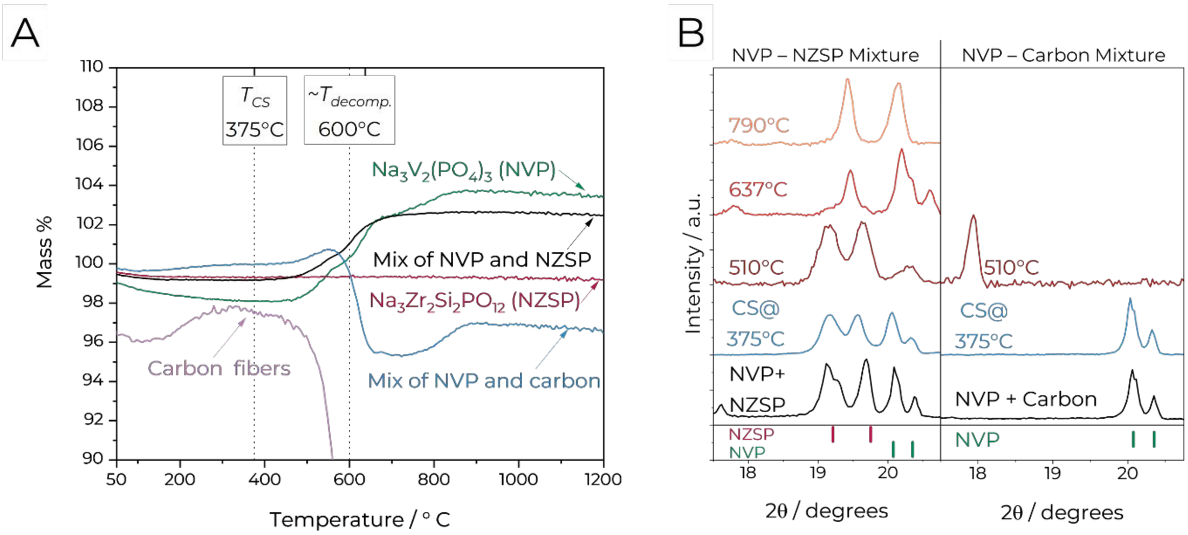

***Figure 2*** *Thermogravimetric data for the pure NVP, NZSP, and carbon are shown in (**A**), alongside a diphasic mixture of NVP-NZSP and NVP-carbon nanofibers (**A**).* $T_{cs}$ *denotes the cold sintering temperature and* $T_{decomp.}$ *denotes the approximate decomposition temperature. XRD data for biphasic mixtures in their as-mixed state (black) and after annealing in air at the labeled temperatures is shown in (**B**). The NVP-NZSP mixture data is shown in the left panel while the NVP-carbon mixture data is shown in the right panel. CS = cold sintering*

## 4.3 Representative microstructures of cold sintered diphasic composites

Having verified with XRD that the cold sintered pellets retained their primary chemical phases, the microstructure of the pellets was investigated with SEM. In our previous report, we showed that the pure NVP material could be cold sintered to approximately 90% relative density using the present conditions (10 vol.% NaOH, 375°C, 350 MPa, three-hour dwell). In this prior study, we noted very little change in the relative density when the conductive additives were introduced. This finding is corroborated here, with the measured relative densities of the NVP-carbon black composites ranging from 91% to 95%, accounting for the volume fraction of carbon in the theoretical density measurement (**Figure S2A**). This insensitivity of the relative density to cold sintered pellet composition is reflected in the NVP-carbon nanofiber and NVP-NZSP composites as well. (**Figure S2B**)

Representative microstructures of the composite pellets are shown in **Figure 3**. In **Figure 3A-B,** a polished surface of a composite containing 5 vol.% of carbon black and 95 vol.% NVP is shown. The sintered ceramic matrix is evident, with flat grain boundaries present throughout the sample. Small pores, on the order of 1 μm, are found within the microstructure as well, which is consistent with the degree of densification measured for these samples. Chemical mapping (**Figure 3B**) reveals the presence of carbon within the majority of the pores. A weak carbon signature can be detected at some grain boundaries, however, the spatial resolution of chemical mapping in EDS/SEM is insufficient to be confident in this observation. The presence of carbon in the grain boundaries is proved using TEM later in this manuscript (**Section 5.3**).

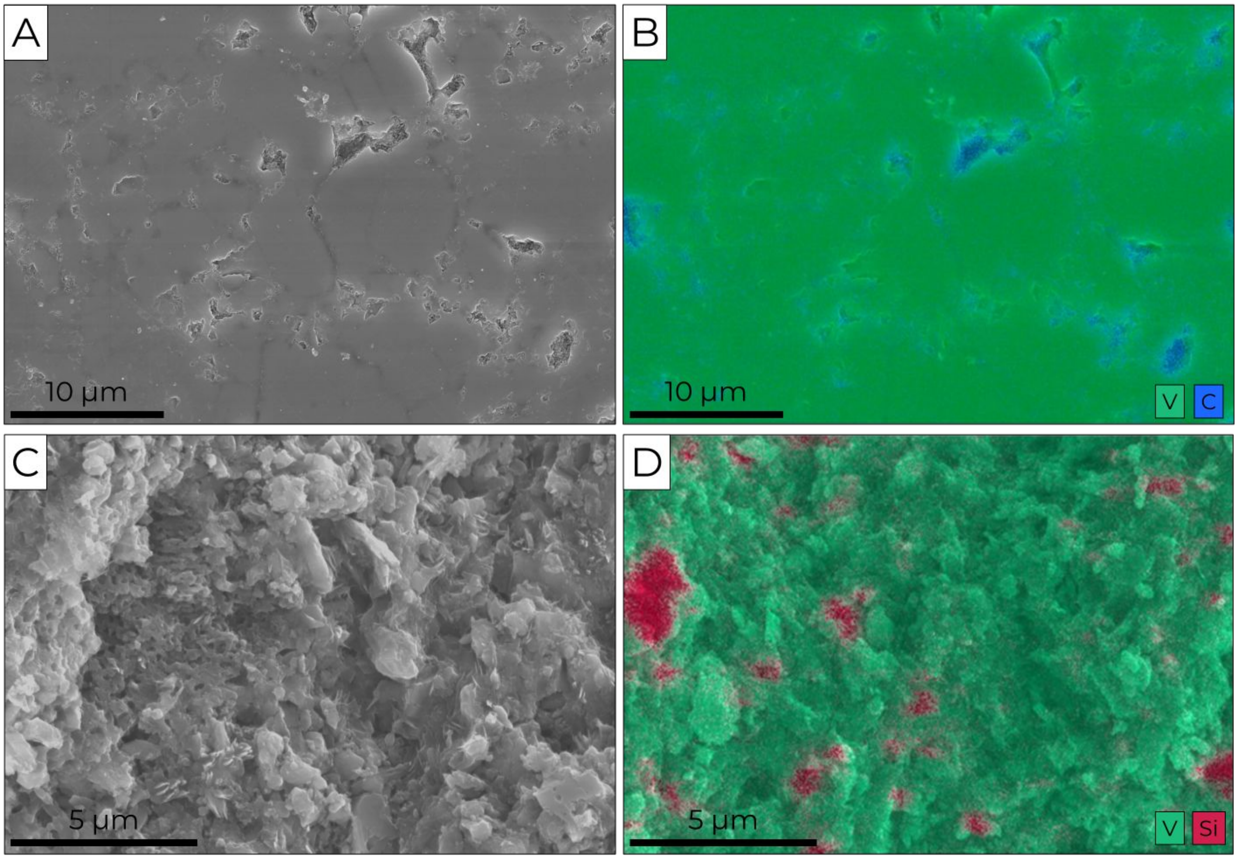

***Figure 3*** *Secondary electron image of a polished surface of a cold sintered sample containing 5 vol.% carbon black and 95 vol.% NVP (**A**) with accompanying EDS mapping (**B**). A fracture surface image of a cold sintered sample containing 40 vol.% NZSP and 60 vol.% NVP (**C**) with accompanying EDS mapping (**D**).*

**Figure 3C-D** depicts the fracture surface of an NVP-NZSP composite (10 vol% NZSP). A similarly dense microstructure is observed, with some smaller grains with an irregular morphology corresponding the NZSP phase (**Figure 3C-D**). These microstructures are consistent with our prior work[67,68] as well as similar studies of low temperature sintering of NZSP ceramics[84]. Collectively, these composite microstructures and diffraction patterns confirm the basis for this study, which is demonstrating that cold sintering can be used to fabricate dense ceramic-matrix composites of materials which would otherwise chemically interact with each other during conventional solid-state sintering. The absence of large amounts of secondary phases and porosity ensure that the electrical measurements represent the properties of a well-sintered diphasic ceramic, which is important in the interpretation of frequency-dependent electrical measurements.

## 5. Conductive properties of carbon black – NVP composites

The previous section demonstrated the ability to fabricate dense diphasic composites at low temperature with minimal thermal degradation by cold sintering. In this section, impedance spectroscopy is performed on a spectrum of diphasic compositions. It is shown that the addition of conductive agents (either carbon or solid electrolyte) increases the total conductivity, and the impedance spectra is interrogated for insight into the relationship between volume of conductive additive and dominant ionic/electronic impedance response. These results not only demonstrate the success of producing conductive diphasic composites but hopefully add insight into future directions of research for measuring the conductive properties of dense, mixed-conducting, composites for solid-state battery research.

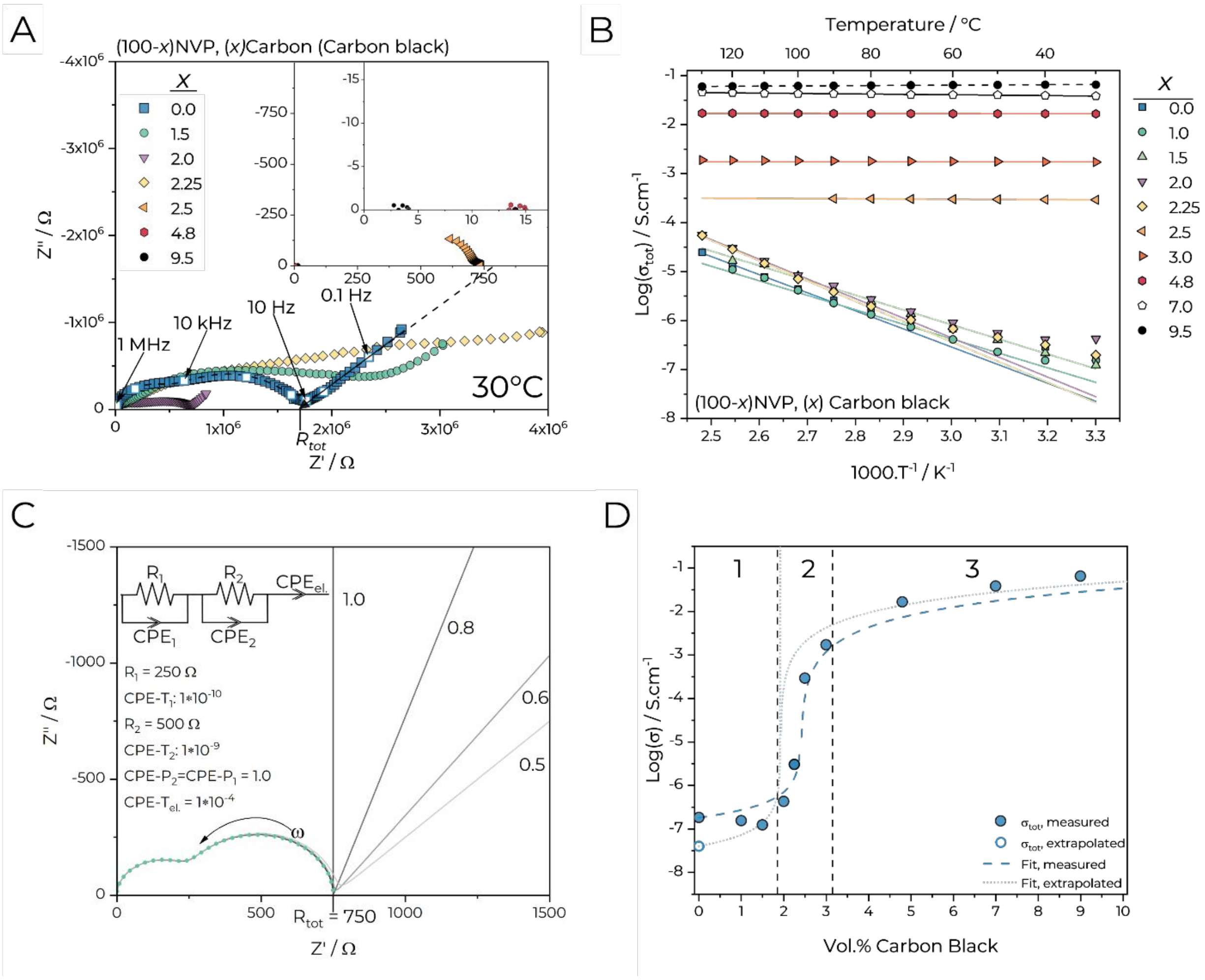

***Figure 4*** *The impedance spectra of numerous NVP-carbon black diphasic composites containing (x)vol.% carbon black, plotted in the complex plane (**A**). An Arrhenius plot of the total conductivity versus inverse temperature for the cold sintered NVP-carbon black composites. Solid lines denote Arrhenius fits from high temperature (130°C-90°C) (**B**). Simulated complex plane representation of the impedance spectra from the inset equivalent circuit. Lines are labelled with corresponding* $CPE_{el}$*-P value, dashed lined* $CPE_{el}$*-T = 0,* $\omega = 2\pi f$ *(**C**).* $\sigma_{tot}$ *for the diphasic composites as a function of vol.% carbon black. Lines fit using percolation equation described in text, with distinct regions labeled. Dashed lines and dotted line use experimentally measured and extrapolated values for* $\sigma_{tot}$ *of the pure NVP, respectively (**D**).*

**Figure 4A** plots the complex impedance (*Z'* v.s. *Z''*) at 30°C of cold sintered pellets ranging in volume percentage of carbon black from 0 vol.% to 9.5 vol.%. In the case of 0 vol.% carbon black (i.e., pure NVP) a total resistance ($R_{tot}$) of $1.74\times10^6$ Ω is found by extrapolating the linear response at low frequency, due to $Na^+$ polarization at the ion-blocking platinum electrode interface, to its intercept with the *Z'* axis, as shown in **Figure 4A** with a solid arrow. The total conductivity of the sample ($\sigma_{tot}$) is then calculated as:

$$\sigma_{tot} = \frac{t}{R_{tot} * A} \tag{1}$$

Where $t$ and $A$ are the thickness of the sample ($cm^{-1}$) and electrode area ($cm^{-2}$), respectively. The resulting $\sigma_{tot}$ for the pure NVP sample at 30°C is thus $1.82\times10^{-7}$ $S.cm^{-1}$, which agrees closely with both our previous work and prior reports of conventionally sintered samples of a similar NVP composition[67,85]. This measurement was repeated up to 130 °C, allowing for the plotting of $\sigma_{tot}$ versus inverse temperature (**Figure 4B**). Plotting the natural log of the $\sigma_{tot}$ versus inverse temperature yields a line with a slope corresponding to the total activation energy ($E_{a,tot}$), which for the pure NVP is 0.79 eV. The pure NVP $\sigma_{tot}$ values deviate from Arrhenius behavior at low temperatures (ca. $T_{EIS} < 80$°C), which has been previously attributed to interaction with atmospheric moisture.[85] Extrapolation of $\sigma_{tot}$ to 30°C yields a conductivity of ca. $4.0\times10^{-8}$ $S.cm^{-1}$, which may more accurately represent the pure NVP ionic conductivity at this temperature. Accordingly, this value is also employed later in the percolation model.

## 5.1 Impedance response and conductivity of the pure cold sintered NVP

The grain ($\sigma_b$) and grain boundary ($\sigma_{gb}$) conductivity of the pure NVP can also be obtained by employing an appropriate equivalent circuit. For polycrystalline ceramics, the separation of the grain and grain boundary resistances, and thus conductivity, is obtained by representing each microstructural feature with a parallel combination of a constant-phase-element (CPE) and resistor.[86] These are then placed in series, followed by an additional CPE element to account for the blocking electrode polarization ($CPE_{el}$), to construct an equivalent circuit (**Figure 4C**, inset) which can be fit to experimental impedance data to obtain values of the apparent grain resistance ($R_1$) and apparent grain boundary resistance ($R_2$), as well as their respective CPE parameters. Using **Equation 1**, we find that at 30°C, $\sigma_b$ and $\sigma_{gb}$ for the pure NVP are $7.36\times10^{-7}$ $S.cm^{-1}$ and $2.52\times10^{-7}$ $S.cm^{-1}$, respectively. The corresponding activation energy values for the grain interior and grain boundary are 0.62 eV and 0.74 eV, respectively. These values are also consistent with NVP sintered by cold sintering and solid-state sintering.[67,85] Plotted in an Arrhenius fashion **(Figure S3)**, the grain interior is linear across the entire temperature regime while the grain boundary resistance mirrors the nonlinearity observed in the total conductivity.

## 5.2 Impedance response and conductivity of diphasic samples containing NVP and carbon black

The equivalent circuits and fitting procedure described in the preceding section was then applied to the composites of NVP and carbon black (**Figure 4A**). We observe three distinct regions of similar impedance responses as the amount of carbon is increased (**Figure 4A** and **Figure 4D**). In **region 1** (vol.% carbon black ≤ 1.5), two semicircles are observed in the complex plane, but the low frequency semicircle appears larger and more dispersed than the corresponding response of the pure NVP sample. For example, upon fitting the spectra to the same equivalent circuit as the pure NVP, $\sigma_{gb}$ of the 1.5 vol.% carbon black sample is $1.27\times10^{-7}$ $S.cm^{-1}$. In **region 2**, from ca. 2.0 to 3.0 vol.% carbon, the low frequency response of the composites becomes difficult to interpret near room temperature (30°C). For the 2.25 vol.% carbon black sample, the impedance response is nearly parallel to the $Z'$ axis at low frequencies, which may be due to either/both an increase in grain boundary resistance ($R_2$) and/or a decrease in the angle formed between the low frequency tail and the $Z'$ axis. The possible physical origins for these effects are discussed later in this section. For this sample (2.25 vol.% carbon black), only a high frequency semicircle can be confidently fit, which is taken as $R_{tot}$ for this sample ($\sigma_{tot} = 3.86\times10^{-6}$ $S.cm^{-1}$, **Figure S4**). It is unclear why the samples containing 2.0 vol.% carbon black consistently produced impedance spectra of slightly higher conductivity than the 2.25 vol.% carbon black samples but retained a similar shape in the complex plane to the pure NVP response. A possible explanation is that the polycrystalline NVP response still dominates the frequency-dependent response at this carbon loading because there are no large connected carbon networks formed yet, but there are enough localized areas of carbon present to greatly reduce the effective volume of pure polycrystalline NVP which must be traversed by a conducting $Na^+$ ion. At a higher loading of carbon (2.5 vol.% and 3.0 vol.%), the sample begins to short circuit and only a high frequency partial semicircle is visible (**Figure 4A, large inset**). In this case, $R_{tot}$ is clearly the low frequency intercept with the $Z'$ axis, which is 750 Ω for the 2.5 vol.% sample. In **region 3**, for volumes of carbon greater than 3%, a complete short circuit is observed (**Figure 4A, small inset**), indicating that there is a continuous pathway for electronic conduction between the two sputtered platinum electrodes applied to either side of the cold sintered composite sample. For these samples, $R_{tot}$ is taken to be the short circuit value (ca. 15 Ω for the 4.8 vol.% sample). Note that only a subset of the impedance spectra for the carbon (carbon black)

– NVP composites are shown in **Figure 4A**. All of the impedance spectra for the NVP-carbon composites (both carbon black and CNF) at 30°C are shown in **Figure S5**.

There are two important trends to make note of. First, the shape of the impedance spectra changes from that of a polycrystalline ceramic to a short circuit as carbon is added. Second, the $\sigma_{tot}$ values, when plotted as a function of vol.% carbon (**Figure 4D**), resembles a classic percolating behavior, namely, once a critical volume fraction of carbon has been added, the total conductivity rapidly rises to nearly that of the pure carbon. To explain these trends, we will now describe the data in each regime in more detail and the most likely physical origins.

Upon the addition of a small amount of carbon (**region 1** in **Figure 4D**), the low frequency semicircle and electrode spike in the impedance spectra become less distinct from each other. There are two likely causes for this effect. The first is a greater dispersion in the grain boundary response, likely arising for the carbon acting to block $Na^+$ diffusion while simultaneously serving as a short-range electron pathway. The second likely cause is an increase in the electron partial conductivity owing to the carbon acting as long-range electron pathways. An increase in the partial electronic conductivity would be expected to decrease the "ion-blocking", i.e., polarizing, behavior at the sample-metal electrode interface. A reduction in the polarization owing to an increase in electronic conduction would result in a smaller angle between the electrode spike and *Z'* axis in the complex plane at low frequencies[87]. This may also explain the observed changes in the low frequency behavior of the samples with small amounts of carbon. These effects are also more pronounced when more carbon is added.

In **region 2**, extended networks of carbon black are formed, introducing pathways for electronic conduction. This has two effects: (1) the total resistance of the composite sample decreases exponentially and (2) a greater portion of the total conductivity can be ascribed to electronic conduction through the carbon black. The first effect is clear from the decreased resistance as more carbon is added. The second effect is evidenced by large changes in low frequency response as more carbon is added. Specifically, the low frequency linear tail described by $CPE_{el}$ transitions from a near 45° angle (relative to *Z'* axis) for the pure NVP to a near horizontal line (2.25 vol%, **Figure 4A**) and is absent for carbon contents ≥ 2.5 vol.%. The impedance response for a generic CPE element is given by:

$$Z_{CPE} = \frac{1}{T_{CPE} * (j * \omega)^{P_{CPE}}} \qquad (2)$$

Where $T_{CPE}$ and $P_{CPE}$ are parameters related to the deviation of the response from an ideal capacitor[88], $j$ is equal to $\sqrt{-1}$, and $\omega$ is the angular frequency ($\omega = 2\pi f$, $f$ = frequency in hertz). $P$ ranges from 0 to 1, with a value of 1 representing a perfect capacitor (i.e., perfectly blocking conditions) and results in a vertical line in the complex plane (**Figure 4C**). Thus, we would expect that the increase in continuous carbon networks in **region 2**, which leads to the decrease in total resistance, would be accompanied by a progressively increasing departure from ideal blocking conditions (i.e., perfect ionic conductor behavior). The effect of this decreasing $P_{CPE}$ value is shown schematically in **Figure 4C** by simulating otherwise identical impedance spectra with a varied $P_{CPE}$ value for the $CPE_{el}$ equivalent circuit element. This hypothesis is consistent with our observations that the increasing amount of carbon is accompanied by first a flattening of the low frequency tail, followed by the absence of a low frequency polarization, and finally a short circuit (**region 3**) of the impedance response when plotted in the complex plane. Note that it is also possible to use the parameters of a CPE element in combination with a resistor to estimate the capacitance of a semicircle, which can be used to identify the physical origins of some impedance responses, such discerning grain from grain boundary responses. However, for many of the composite samples, the $P_{CPE}$ values are much smaller than one, which renders the capacitance estimations less accurate, as the responses deviate further from an ideal capacitor. For this reason, the capacitances values are only used later in this manuscript (**section 6.1**) where a new interfacial response is identified and discussed.

Finally, in **region 3**, the resistance of the sample is constant for the entire frequency range, i.e., the sample is essentially shorted and produces only a dc resistance. This results from the electrical current flowing completely through a well-percolated carbon network within the dense ceramic matrix, shunting the ionic current previously observed at low loadings of carbon black. These dc resistance values have little dependence on temperature (**Figure 4B**), with activation energies around 0.01 eV, which is consistent with electronic conduction through carbon.[89]

## 5.3 The total conductivity of the ceramic-carbon composites conforms to classic percolation theory

Percolation theory has been well-developed for diphasic insulator-conductor systems such as carbon in resin or metal embedded in ceramics.[90–92] In this case, the diphasic system contains carbon embedded within a sintered ceramic matrix, fabricated in one-step by cold sintering. It stands to reason that, despite the novel method of fabrication for the present system, the resulting diphasic composite should conform to the general percolation equation given by:

$$\sigma_{tot} = \sigma_i * \left(1 - \frac{f}{f_c}\right)^t \tag{3}$$

Where $\sigma_{tot}$ is the total conductivity of the composite, $\sigma_i$ is the conductivity of the end member phase $i$, $f$ is the volume fraction of phase $i$, $f_c$ is the percolation threshold of phase $i$, and $t$ is the critical exponent. By letting the bounding conductivity of the phases ($\sigma_i$) be the measured $\sigma_{tot}$ at 30°C for the pure NVP at low amounts carbon, and the approximate electronic conductivity of carbon (1 S.cm$^{-1}$) at high amounts of carbon for the system, **Equation 3** may then be numerically solved to obtain $f_c$ and $t$ for the diphasic system, resulting in $f_c$ = 2.4 vol.% and $t$ = 0.75 (**Figure 4D**, solid line). To account possibility of the non-Arrhenius behavior of the pure NVP near room temperature, we also solve the percolation equation with $\sigma_{tot}$ (0 vol.% carbon black) equal to $4.01\times10^{-8}$ S.cm$^{-1}$ (**Figure 4D**, dashed line), which yield slightly different $f_c$ and $t$ values (1.9 vol.% and 0.82, respectively).

In this latter case, the fit of **Equation 3** to the high and low vol.% range improves but the fit in the percolation region is less accurate. In the former case, by contrast, the percolation region is fitted quite well with some accuracy lost in the low and high vol.% carbon black regions. Thus, while we previously noted that the impedance spectra at 30°C seemed to imply an increase in $R_{gb}$ when carbon black was added, suggesting that the carbon acted as a barrier to Na$^+$ through the grain boundaries, it is difficult to separate these effects from the non-Arrhenius behavior without further information or additional experiments.

Percolation theory predicts that $f_c$ should be in the range of 10-15 vol.% for isotropic fillers.[93] Carbon black is characterized by a spherical morphology, so we would expect that it behaves as an isotropic filler in this diphasic system. However, as shown in the previous paragraph, fitting the percolation equation (**Equation 3**) to suggests that $f_c$ for this system lies in the range of

1.9 to 2.4 vol.%, which is much lower than expected. To ascertain how cold sintering was generating percolation at such low loadings of carbon we performed cryogenic TEM on diphasic samples containing the NVP active material and carbon black (**Figure 5**).

Between some grains of NVP, we observe relatively wide (28 ± 4 nm) amorphous grain boundary regions, which also appear to contain spherical particles of carbon black (Ø = 16 ± 3 nm) (**Figure 5A**). Using elemental mapping, we confirm that these regions are dominated by carbon (**Figure 5B**). In addition to these grain boundaries, we also observe much thinner grain boundary regions (**Figure 5C**), which are unable to accommodate the carbon black particles and thick carbon films observed in the thicker grain boundary regions. However, imaging these grain boundaries at high resolution reveals a thin amorphous region (thickness less than 2.5 nm) which can also be attributed to carbon, suggesting that the carbon black shears during the powder mixing step, resulting in carbon being present at the majority of grain boundaries in the composite samples. This is consistent with prior studies of the structure of carbon black, which have identified a turbostatic surface layer prone to thinning and dispersion.[76] This observation explains the low $f_c$ value measured for this diphasic system; the presence of a carbon coating at the interfaces between the grains, generated by the high shear planetary mixing process, increases the ceramic-carbon interfacial area within the sample, yielding a system with a higher probability of forming a percolated network at low volume loadings. This carbon coating does not appear to impede the cold sintering process from promoting densification, as carbon can even be observed in triple-point regions (**Figure S6**) and the relative densities of all the samples remain above 88% (**Figure S2**). Finally, this carbon coating cannot be derived solely from the sol-gel synthesis process because if this were the case then cold sintered pellets of pure NVP would also exhibit only electrical conduction.

This observation of a ubiquitous thin carbon coating at the grain boundary regions also may help explain the low frequency impedance response of the samples with only small amounts of carbon. If this coating is generated on many grain boundaries even when the carbon loading is only in the range of 1 vol.%, it is possible that the loss in grain boundary semicircle distinction in the complex plane of the impedance is related to the partial $Na^+$ blocking effect of the carbon layers as well as the introduction of electronic conduction at these grain boundary regions. Still, however, additional experiments such as single grain boundary impedance measurements[94], may be required to unequivocally prove this explanation.

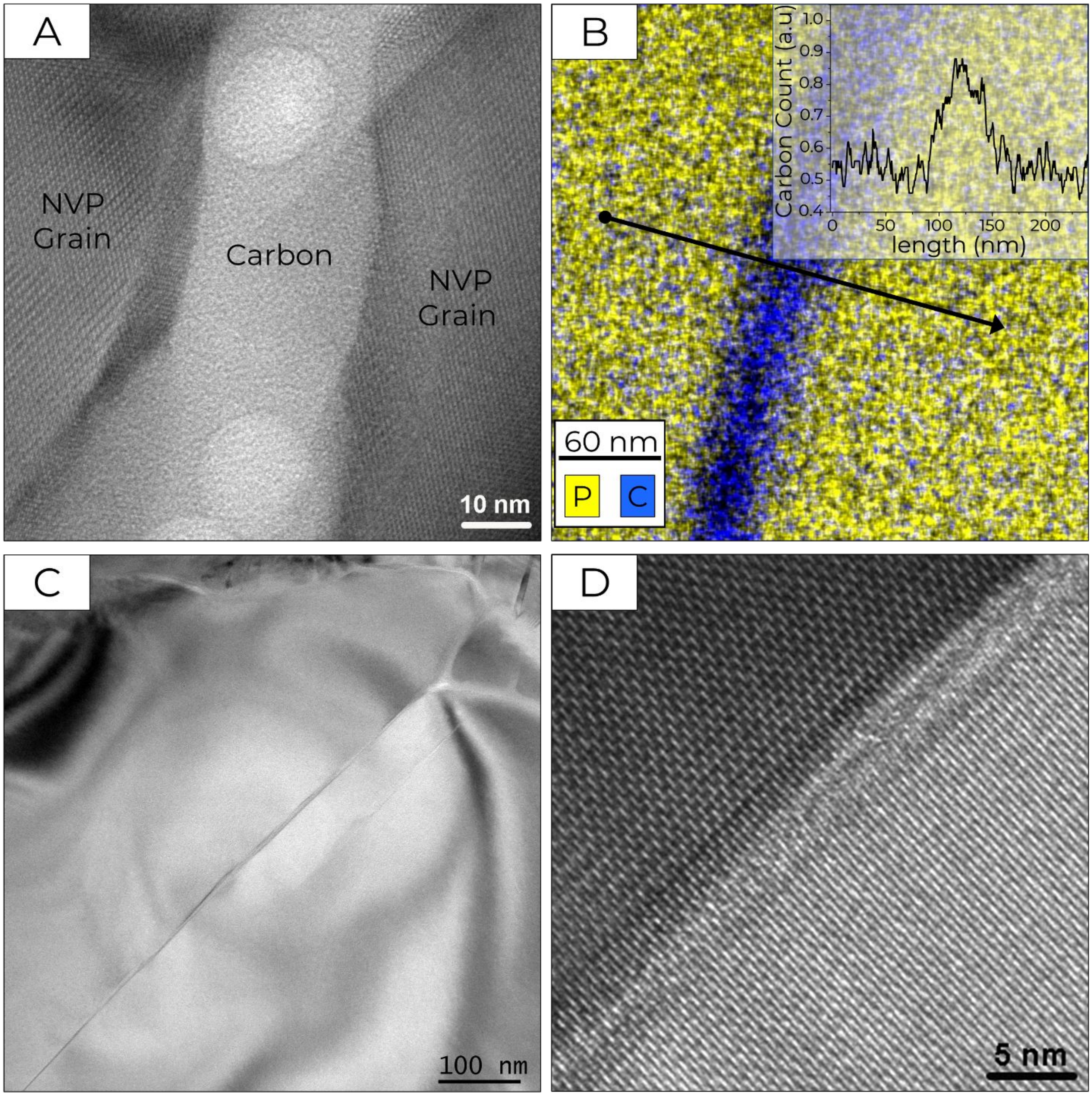

***Figure 5*** *Cryogenic TEM images of a composite containing 5 vol.% carbon black, depicting a wide grain boundary decorated with amorphous and structured carbon (**A**). A chemical mapping of a representative grain boundary containing carbon, and the associated line scan (**B**). A grain boundary much thinner than that depicted in (A), but in which atomic resolution reveals a thin layer of carbon between the adjacent grains (**C-D**).*

## 5.4 Conductive properties of carbon nanofiber – NVP diphasic composites

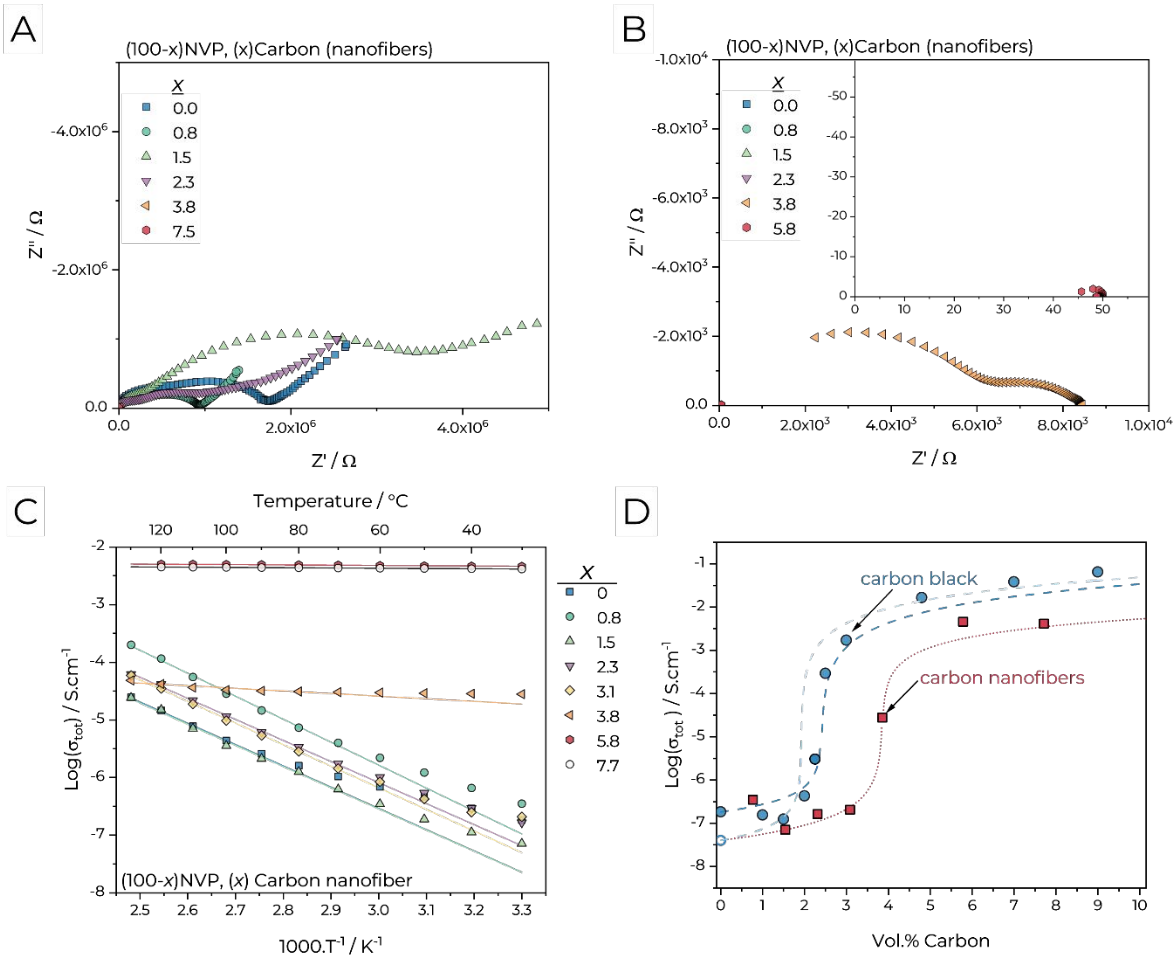

***Figure 6*** *Complex plane representation of the impedance spectra at 30°C for diphasic composites containing (x) vol.% of carbon nanofiber and (100-x) vol.% of NVP (**A-B**). The logarithm of $\sigma_{tot}$ of the diphasic NVP-CNF composites versus inverse absolute temperature (**C**). Log($\sigma_{tot}$) of the NVP-carbon diphasic composites plotted as a function of vol.% carbon, with the lines indicating the respective fitting of the percolation equation described in the text (**D**).*

For comparison, we fabricated a second series of diphasic samples containing NVP active and carbon, but in this case employed a high aspect ratio carbon nanofiber instead of carbon black. This series of diphasic samples provides an interesting contrast to the previously discussed carbon black – NVP samples, given that the high aspect ratio of the carbon nanofibers (CNF) was expected to generate percolation at a lower volume fraction than the isotropic carbon. The approximate aspect ratio of the CNFs is 90, estimated from the manufacturers stated average fiber length (35 µm) and fiber diameter (0.4 µm).

The impedance spectra at 30°C of the diphasic samples are shown in **Figure 6A** and **Figure 6B**. In general, the impedance response of the NVP-CNF composites is similar to that of the carbon black. As a small amount of CNF is added, the distinction between the low frequency semicircle and the linear electrode polarization is lost, similar to the trend observed in the carbon black samples. Once ca. 3.8 vol.% CNF is added, $\sigma_{tot}$ increases rapidly and the electrode polarization is completely lost (**Figure 6B**). This appears to be the percolation threshold for this diphasic system, with the resulting impedance being characterized by two semicircles in the complex plane. $R_{tot}$ is once again defined as the low frequency $Z'$ intercept, similar to the 2.25 vol.% carbon black sample (**Figure 4A, large inset**), and does not change appreciably with temperature (**Figure 6C**). Finally, for samples with more than 3.8 vol.% CNF, a pure short circuit response is observed, similar to the carbon black samples (**Figure 6B, inset**).

Plotting $\sigma_{tot}$ against inverse temperature (**Figure 6C**) shows that the composites also exhibit generally Arrhenius behavior at high temperature ($T_{EIS} \geq 70°C$), with some deviation from linearity at the lowest temperatures, which is similar to what was observed in the carbon black composites. Similarly, plotting $\sigma_{tot}$ as a function of volume fraction (**Figure 6D**) shows a relatively low conductivity before the percolation threshold which may also indicate that the carbon nanofibers act as a barrier to $Na^+$ diffusion. By fitting $\sigma_{tot}$ for the CNF samples to the percolation equation (**Equation 3**), a percolation threshold ($f_c$) of 3.8 vol.% CNF and an exponent ($t$) of 1.11 is obtained. The model fits the data quite well when we employ a $\sigma_{tot}$ for the pure NVP extrapolated from high temperature, as described in the previous section. Interestingly, a percolation threshold of 3.8 vol.% CNF is larger than the ca. 2 vol.% percolation threshold observed for the carbon black. In the previous section, we attributed the low $f_c$ of the carbon black samples to sheared carbon at the grain boundaries, so this effect appears to be absent in CNF-NVP diphasic composites. Thus, the difference in surface properties of these distinct forms of carbon contributes to the ultimate behavior of the diphasic composites, which may be an important aspect to consider in future studies concerned with optimizing the use of carbon in composite electrodes.[89,95,96]

## 5.5 Implications for dense ceramic-carbon composites in solid-state battery design

The individual findings described thus far with respect to the carbon-NVP diphasic composites provide some potential insight in solid-state battery electrode design. First, the volumetric loadings of carbon required to generate percolated networks is much lower than the typical loadings in laboratory-scale electrode compositions. It is common to add between 10 to 25 wt.% of carbon to such solid-state electrode compositions[76,97], which in this model system would correspond to ca. 18 to 40 vol.% carbon. The disparity between the amount of carbon required to induce a percolated response in the system and that required for electrochemical cycling is thus striking and has yet to be fully rationalized. One explanation is that, at the very onset of percolation, only fraction of the active material is practically accessible to the percolated carbon network, with a more extensively percolated network of carbon pathways being required to make full use of the complete active material loading. However, if the electrical response of a sample which is barely percolated (e.g., 4.8 vol.% carbon black) appears nearly identical to one with considerably more carbon (e.g., 9.5 vol.% carbon black), then it will be difficult to study the relationship between the observable bulk properties of carbon-ceramic diphasic composites and their electrochemical performance without actually evaluating the composites in electrochemical cells. Thus, a comprehensive understanding of the relationship between amount of carbon, electronic conductivity, and expected electrochemical performance will necessitate multiple characterization techniques, such as impedance spectroscopy, dc resistance measurements, and electrochemical cycling. This is an interesting avenue for future work. It should also be noted that the high shear mixing process and the cold sintering process itself may play a role in generating percolated networks of carbon at low volumetric thresholds. Without comparing these results to other samples producing using different mixing methods or other means of densifying the composites, it is not possible to consider this possibility further in this work.

It may also be important to understand both the electron and ion conduction properties across the entire composition range. The results presented here point to a decrease in $Na^+$-$\sigma_{gb}$ at low carbon loadings which likely persists at higher loadings of carbon but is obfuscated by the increase in electronic conduction through the carbon network. The use of electron-blocking, ion-conducting electrodes, such as an $Na^+$-conducting polymer electrolyte, may allow for measurements of the ionic conductivity for systems with percolated carbon networks, but the collection and interpretation of this data is difficult and imprecise without careful benchmarking.[87]

It is worth briefly discussing the notion of partial conductivity in mixed conductors and its relationship to the bulk observed total conductivity, the latter being the emphasis of this study. The observed total conductivity is a volume-fraction weighted summation of several partial conductivities. For an ideal brick layer model of a perfectly ionically conducting polycrystalline ceramic, the total conductivity would be the sum of the ionic grain and ionic grain boundary conductivity. The samples presented in this study are not ideal, however, and there are several factors which prevent us from measuring the individual partial conductivities in each sample. For example, in a sample with a percolated network of carbon, impedance measurements with metallic electrodes exhibits only the resistance related to electron conduction through the carbon network, and not the resistance related to ionic conduction within the sample (which would require ionically conducting and electronically blocking electrodes). Thus, we have deliberately avoided applying a partial conductivity analysis framework to the impedance measurements, as the emphasis of this study was the observed total conductivity from impedance analysis of solid-state battery composites using the most common form of electrode (ion-blocking metal electrodes). However, a similar study of mixed conducting composites where the partial conductivities are measured and compared to the observed total conductivity would be an interesting avenue of future work.

Finally, these results demonstrate the importance of the type of carbon used and the methods used to disperse said carbon. It is possible that a lower energy mixing may prevent the shearing behavior observed in the carbon black, yielding a system with a higher percolation threshold as theory would predict. However, this may not be desirable as numerous prior studies have demonstrated that carbon coatings on active materials are beneficial for driving redox reactions at high rates.[98–100] Thus, these findings suggest that similar carbon-ceramic systems for solid-state batteries will likely have to contend with competing design aspects, namely balancing the trade-offs between carbons that disperse easily to form percolated electronic networks at low volume fractions, but which simultaneously introduce $Na^+$ diffusion barriers which are difficult to measure using conventional techniques.

## 6. Conductive properties of NZSP solid electrolyte and NVP diphasic composites

In this section, a series of diphasic composites containing a varying amount of NZSP solid electrolyte is subjected to impedance spectroscopy. The results demonstrate a gradual increase in conductivity across the compositional spectrum, as opposed to the percolation behavior observed in the previous sections. An interfacial contribution to the impedance response is also discerned and investigated by its response to increasing dc bias.

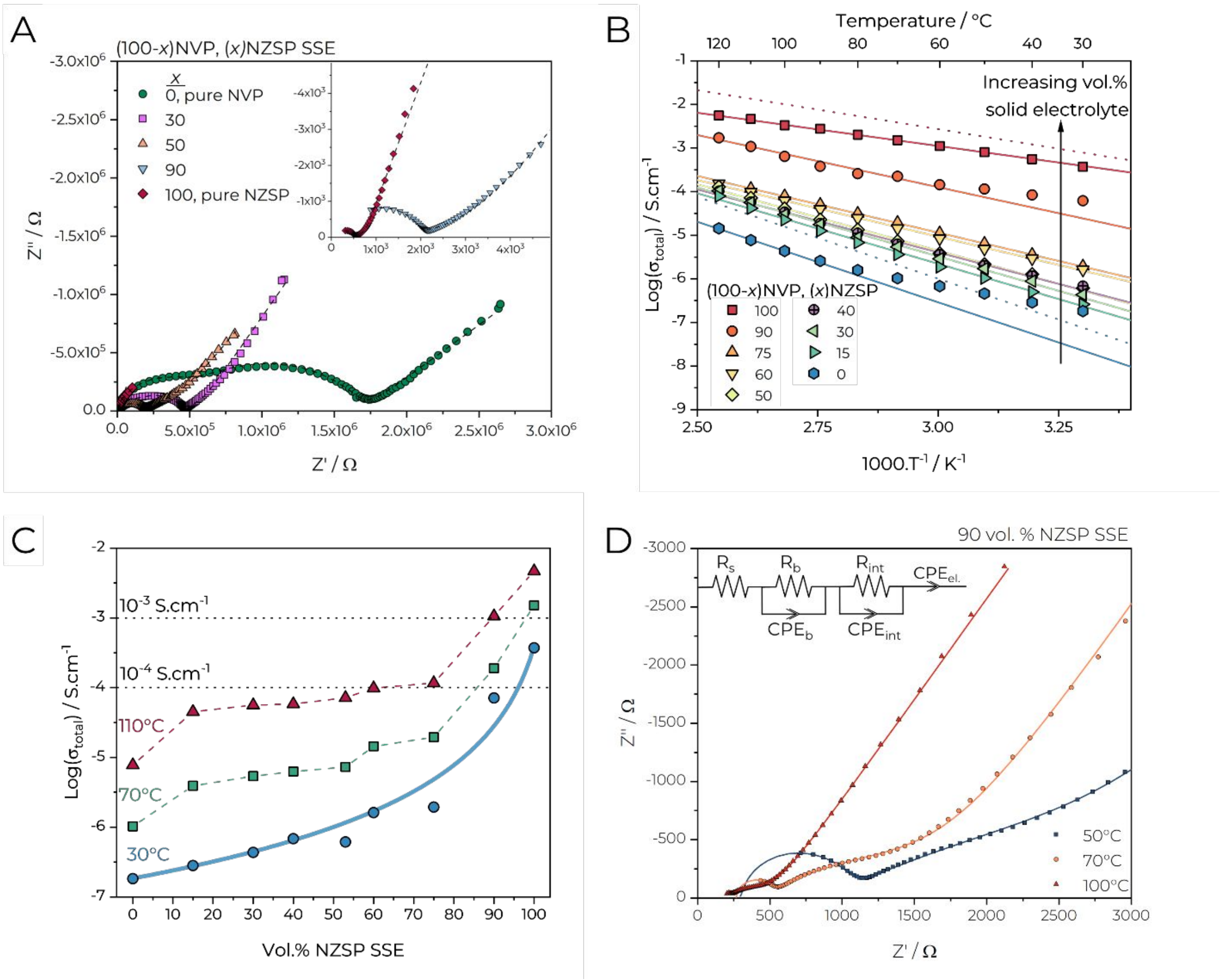

*Figure 7 Complex plane representation of the impedance spectra at 30°C for diphasic composites containing (x) vol.% of NZSP solid electrolyte and (100-x) vol.% of NVP (**A**). Log($\sigma_{tot}$) of the diphasic NZSP-NVP composites plotted as a function of inverse absolute temperature. Solid lines indicate Arrhenius fits to the respective data set, dashed lines depict the $\sigma_{tot}$ values of conventionally processed NVP[85] (blue) and NZSP[68] (red) (**B**). Log($\sigma_{tot}$) of the diphasic NZSP-NVP composites plotted as a function of vol.% NZSP. Solid line denotes mixing law fit; dashed lines are a guide to the eye (**C**). The complex plane representation of the impedance spectra for a sample containing 90 vol.% NZSP, 10 vol.% NVP at three temperatures demonstrating the presence of an interfacial response. The modified equivalent circuit and its fitting to each spectra (solid lines) are also shown (**D**).*

We now examine a markedly different diphasic system, namely a co-sintered composite of the ceramic NVP active material and a ceramic NASICON solid electrolyte ($Na_3Zr_2Si_2PO_{12}$, NZSP). The impedance spectra of a series of cold sintered pellets containing an increasing volume fraction of the NZSP solid electrolyte is shown is **Figure 7A**. $R_{tot}$ is obtained by extrapolating the low frequency electrode response to the $Z'$ axis, as described previously. The total conductivity of the diphasic composites, $\sigma_{tot}$, is similarly found using **Equation 1**. By following this procedure,

$R_{tot}$ for the pure NZSP sample is 704 Ω, resulting in $\sigma_{tot} = 2.47\times10^{-4}$ S.cm$^{-1}$. This value is consistent with our previous investigation of cold sintering NZSP with sodium hydroxide[68] and is close to the range of conductivities typically reported for NASICON solid electrolytes sintered by other methods. By plotting $\sigma_{tot}$ versus inverse temperature (**Figure 7B**), we find $E_{a,tot}$ for the pure cold sintered solid electrolyte to be 0.30 eV, which also agrees with the prior work.

Alongside the 30°C impedance of the pure NZSP and NVP samples, **Figure 7A** also plots the impedance response for a representative subset of samples containing a diphasic mixture of the NVP active material and the NZSP solid electrolyte, increasing from 30 to 90 vol%. The $R_{tot}$ value for each sample decreases as the volume percent of solid electrolyte in the sample is increased, consistent with the expectation that an increase in the amount of the ionically conductive phase would result in an increase in the total ionic conductivity of the bulk. Specifically, at 30°C, the 30, 50, and 90 volume percent solid electrolyte have total conductivity values of $4.35\times10^{-7}$, $6.14\times10^{-7}$, and $6.20\times10^{-5}$ S.cm$^{-1}$, respectively. It is also worth noting that the angle created by $CPE_{el.}$ and the $Z'$ axis increases as solid electrolyte is added, suggesting a more blocking sample-electrode interface, which would be expected from the increase in conductivity being attributed to additional $Na^+$ conduction, as discussed in **section 5.2**. This is in contrast to the previous observation of a decrease in the angle of $CPE_{el.}$ when carbon was added to NVP, which was attributed to the increase in electronic conduction resulting in a non-blocking sample-electrode interface.

Additionally, we measured the $\sigma_{tot}$ of these diphasic samples from 120°C to 30°C (**Figure 7B**). Clearly, all samples demonstrated Arrhenius behavior with respect to temperature, with the only notable exceptions being the low temperature data for the pure NVP, as discussed previously, and the low temperature $\sigma_{tot}$ of the 90 vol.% NZSP sample. The $E_{a,tot}$ values for this series of diphasic samples decreases quickly from 0.79 eV (pure NVP) to 0.64 eV when only 15 vol.% NZSP is added, decreases slightly to 0.52 eV as the vol.% of NZSP is increased to 75, followed by a sharp decrease to 0.48 eV at 90 vol.%. $E_{a,tot}$ for the NZSP-NVP and the carbon-NVP diphasic composites is plotted as function of vol.% in **Figure S7**.

The total conductivity of the diphasic samples as function of volume percent solid electrolyte is plotted in **Figure 7C**. For the 30°C values, the total conductivity (plotted on a logarithmic scale) rises roughly parabolically with an increasing amount of solid electrolyte. This second-order relationship between the conductivity is often observed in diphasic systems, where both end members contribute meaningfully to the bulk conductivity. Logarithmic mixing laws are often employed to describe such the relationship[90],

$$\sigma_{tot}^{n} = (f * \sigma_1^n) + ((1 - f) * \sigma_2^n) \tag{3}$$

Where $f$ is volume fraction of phase 1 in the composite, $\sigma_1$ and $\sigma_2$ are the conductivities of the diphasic material constituents, and $n$ is the characteristic exponent, ranging from -1 to +1. This model fits the 30°C data well, with an $n$ exponent of 0.38, demonstrating a potentially useful relationship for estimating the conductivity of a diphasic mixture of these two materials at any volume fraction at 30°C (**Figure 7C**, solid line). However, when the total conductivity of the composites is plotted for elevated temperatures, the relationship between composition and conductivity is no longer well-described by a second-order relationship. At both 70°C and 110°C, $\sigma_{tot}$ of the diphasic samples increases quickly once a small amount of NZSP is added, followed by a slow increase from ca. 15 vol.% to 75 vol.%, while additional NZSP beyond 75 vol.% results in a rapid increase in total conductivity towards the pure NZSP upper bound.

First, this observation illustrates how a simple model such as the logarithmic mixing law might be only applicable under certain circumstances, such as low temperatures. Secondly, given the previously noted non-Arrhenius behavior of the pure NVP, the true trend in conductivity at 30°C may be more similar to the high temperature data but is obfuscated by the high $\sigma_{tot}$ from the interaction of the pure NVP with the atmospheric moisture. As the temperature is increased, additional electrical features become more prominent, as will be discussed below, and these additional factors result in complex behavior which defies a simple two parameter model. The question, therefore, becomes what additional factors must be accounted for in order to describe the trend in composite conductivity as solid electrolyte is added to the active material matrix. One obvious potential contribution is the interfacial resistance between the NZSP and NVP. Often, this interfacial response dominates the composite response and usually imparts high resistance to the sample, however there are also numerous reports of an increase in conductivity arising from interfacial regions.[101,102]

## 6.1 A potential interfacial impedance response in co-sintered ceramic composite

In the present diphasic system, there is no salient, dominating interfacial response in the impedance response for most of the samples, however, we do note the appearance of an additional semicircle at low frequencies of the 90 vol.% NZSP sample (**Figure 7D**). We hypothesized that this semicircle corresponded to the NVP-NZSP interface for multiple reasons. First, it is possible to estimate the capacitance of a semicircle in the complex plane by fitting the impedance spectra to a resistor in parallel with a CPE, thereby obtaining $R$, $T_{CPE}$, and $P_{CPE}$, allowing for the estimation of the capacitance ($C$, F.cm$^{-1}$) by:

$$C = \frac{(T_{CPE} * R)^{\left(1/P_{CPE}\right)}}{R} \tag{4}$$

Following this procedure for the impedance spectra of the 90 vol.% sample at 50°C, we obtain an approximate capacitance of $7.5\times10^{-11}$ F.cm$^{-1}$ and $9.52\times10^{-8}$ F.cm$^{-1}$ for the high frequency and low frequency semicircle, respectively. For comparison, at 50 °C, the capacitance associated with grain interior of the pure NVP at 50°C is $2.05\times10^{-12}$ F.cm$^{-1}$ while the NVP grain boundary has a capacitance of $2.28\times10^{-11}$ F.cm$^{-1}$, and the capacitance of the cold sintered pure NZSP grain boundary response is $3.97\times10^{-10}$ F.cm$^{-1}$. Thus, the low frequency semicircle of the 90 vol.% NZSP sample has a capacitance at least three orders of magnitude larger than each of the three most likely alternative microstructural explanations. It has been previously shown that assignment of various impedance responses to microstructural features can be aided by noting the range in which the capacitance of the response falls in, with values smaller than $10^{-9}$ F being associated with bulk and grain boundary responses, while values larger than this are often associated with surface layers or material interfaces[86]. For this reason, we label this second semicircle as $R_{int.}$ and $CPE_{int.}$ in the equivalent circuit depicted in **Figure 7D**. In addition to this modification, we also must add a resistor before the high frequency semicircle ($R_s$) to account for high frequency responses such as the NZSP grain interior. The high frequency semicircle remains labeled $R_b$ and $CPE_b$, but it should be noted that this can no longer be strictly ascribed to the grain interior or grain boundary of the NVP or NZSP phase without additional information.

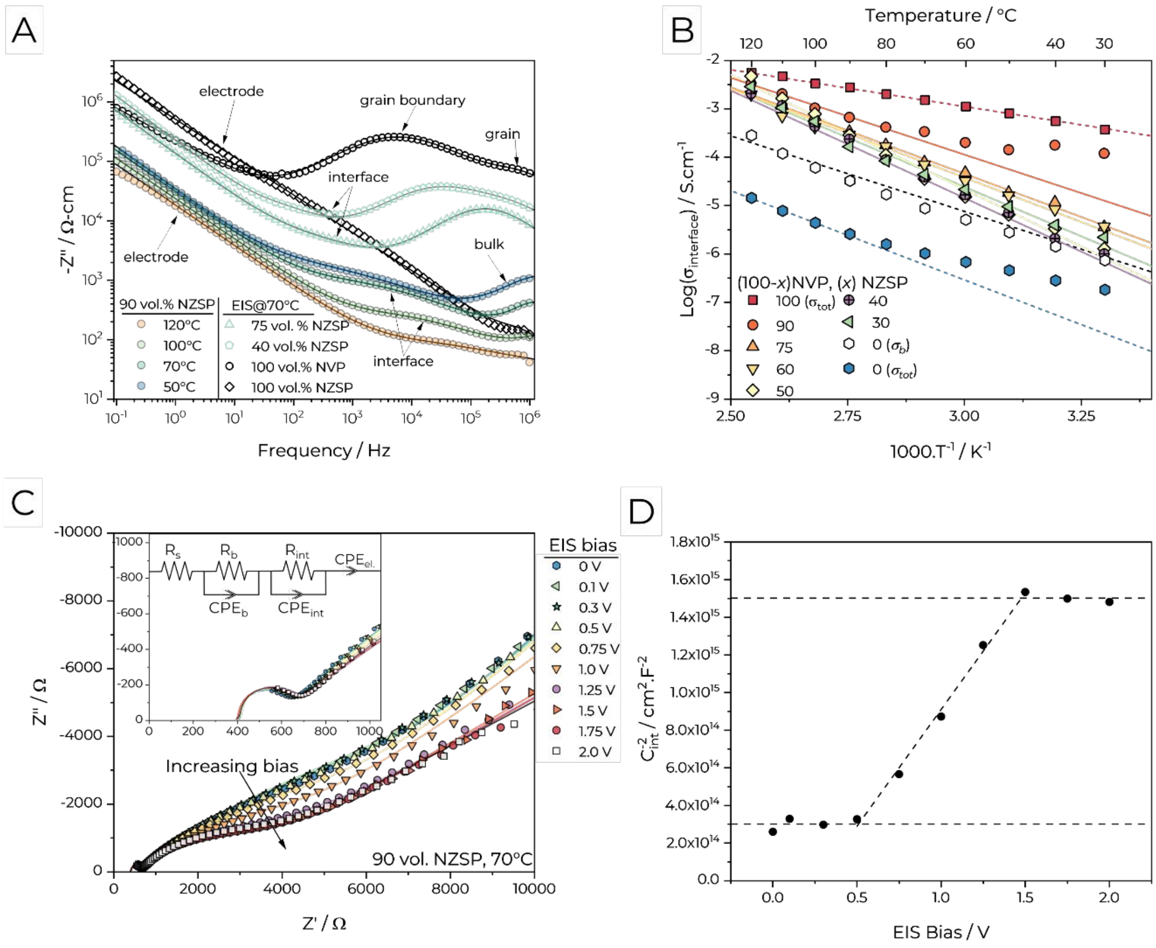

***Figure 8*** *The impedance as a function of frequency is plotted on a log-log scale for numerous diphasic NZSP-NVP samples at various temperatures, with their associated equivalent circuit fitting (solid lines). (**A**) Log($\sigma_{int}$)is plotted against inverse temperature, with the lines representing linear fits to the data. (**B**) The impedance of a 90 vol.% NZSP sample taken at 70°C at increasing dc potentials is shown in (**C**). The associated equivalent circuit and high frequency data is shown in the inset. The inverse square of so-fitted $C_{int}$ as a function of dc potential is shown in (**D**). The linear regime is fit with dashed line and each bounding plateau is averaged and represented with a dashed line.*

With these modifications to the equivalent circuit, the quality of the fit for the 90 vol.% NZSP sample is excellent across the entire frequency range and temperature range (**Figure 8A**). Furthermore, this equivalent circuit containing an interfacial contribution at the intermediate frequencies can also be applied to samples with less NZSP, such as 75 and 40 vol.% NZSP as shown in **Figure 8A**, where the interfacial response is not as easily deconvoluted from the other contributions. In fact, high quality fits to the impedance spectra of these samples with < 90 vol.% NZSP can only be obtained when the interfacial response is included in the equivalent circuit but is difficult to fit owing to the large resistance contributions from the other elements of the sample, such as the NVP grain boundary. Deconvolution of the interfacial contribution to the impedance is therefore accomplished by assuming that the equivalent circuit fitting parameters (e.g., the $T_{CPE}$ and $P_{CPE}$ values of $CPE_{int.}$) are relatively consistent between samples and for small changes in temperature, allowing for the careful fitting of these subtle features[103]. Utilizing the equivalent circuit parameters from the 90 vol.% NZSP impedance fitting as starting estimations for the interfacial contribution in samples of different compositions allows for the determination of $R_{int.}$ for a wide range of samples and temperatures (**Figure 8B**). By fixing these values and allowing $R_{int.}$ to vary, excellent fits to the impedance data can be obtained and thus $\sigma_{int.}$ can be found for nearly all the samples across a wide range of temperatures (**Figure 8B**).

Plotted versus inverse temperature, it is clear from **Figure 8B** that properties of the interfacial response are consistent between samples over a wide compositional range. At 30°C, $\sigma_{int}$ is between $3.67\times10^{-6}$ S.cm$^{-1}$ and $1.01\times10^{-6}$ S.cm$^{-1}$, with only the 90 vol.% NZSP sample having a significantly higher value ($1.20\times10^{-4}$ S.cm$^{-1}$). At 130°C, all of the $\sigma_{int.}$ values approach approximately the same conductivity, ca. $3\times10^{-3}$ S.cm$^{-1}$. Thus, at low temperatures $\sigma_{int}$ is quite close to the conductivity of the NVP grain interior ($\sigma_b$) at 30°C and, as the temperature rises, $\sigma_{int}$ approaches the total conductivity of the NZSP solid electrolyte ($\sigma_{tot.}$), both plotted for reference in **Figure 8B**. The bounding of the interfacial conductivity by the two constituting phases also supports the assignment of this response to the NVP-NZSP cold sintered interface. Further, $E_{a,int.}$ for all of the samples is fairly high, ranging from 0.94 to 0.71 eV, which is also characteristic of Mott-Schottky type interfaces. (**Figure S7A**)

Finally, we sought to unequivocally demonstrate that this new impedance response exhibited Mott-Schottky type interfacial properties as a function of applied voltage, in order to rule out other possible explanations for this response. It is well-known that Mott-Schottky barriers display a linear relationship between the reciprocal of the square of interfacial capacitance ($C_{int.}^{-2}$) and voltage, owing to the space-charge layer generated on either side of the semiconducting barrier.[104] One way of measuring the relationship between the capacitance and applied potential is to measure the impedance of a sample under the influence of increasing dc biases, thereby allowing one to obtain the impedance spectra as a function of voltage. The resulting impedance spectra can then be fit, $C_{int.}$ obtained as described previously, and finally plotted as $C_{int.}^{-2}$ versus the voltage upon which the impedance signal was superimposed (**Figure 8C-D**). This experiment was conducted on the sample containing 90 vol.% NZSP, with impedance measurements taken at a static temperature of 70°C. This temperature was chosen because the high frequency semicircle is still large enough to fit while the intermediate frequency (interfacial) semicircle and the low frequency electrode polarization are still distinct features of the impedance spectrum (which is not true at lower temperatures). **Figure S8** shows the impedance spectra of this sample from 30°C to 120°C to emphasize this point. **Figure 8C** illustrates how the partial semicircle corresponding to the interface response changes as the potential is increased, while the high frequency semicircle and $R_s$ values do not change appreciably. A clear linear regime of $C_{int.}^{-2}$ can be observed between 0.5 and 1.5 V (dc), providing additional support for the assertion that this response can be attributed to a semiconducting interface generated during cold sintering. The absence of change for the high frequency semicircle and $R_s$, on the other hand, suggests that these features correspond to bulk responses in the composite samples.

## 6.2 Potential general implications of the cold sintered diphasic solid electrolyte-electrode system

These findings point to numerous routes for future research and practical considerations for the model system. First, if we assume that practical electrochemical performance of solid-state batteries requires total conductivities ($\sigma_{tot}$) in the range of liquid electrolytes ($10^{-4}$ to $10^{-3}$ S.cm$^{-1}$), it is natural to ask for what compositions and/or temperatures does the NVP-NZSP diphasic system reach these total conductivities?

A composite containing 90 vol.% NZSP and 10 vol.% NVP attains a $\sigma_{tot}$ of only $7.1 \times 10^{-5}$ S.cm$^{-1}$ at 30°C, which is impractical not only for the amount of the volume which is dedicated to solid electrolyte but also for the total conductivity obtained. At 130°C, a sample of 75 vol% NZSP is close to reaching a $\sigma_{tot}$ of $10^{-4}$ S.cm$^{-1}$, but an additional ~15 vol.% solid electrolyte would be required to obtain a $\sigma_{tot}$ of $10^{-3}$ S.cm$^{-1}$. These volume fractions also do not account for the carbon additive, which we demonstrated earlier must be at least in the 2-4 vol.% range. Thus, the combination of the small amount of active material loading and operating temperature requirements render the model system, in its present form, highly impractical. However, the results do suggest pathways forwards, such as the selection of an electrochemical active material with an intrinsically high ionic conductivity and/or the modification of the diphasic system particle morphologies/sizes to increase the rate at which $\sigma_{tot}$ of the composites rises with the volume fraction of solid electrolyte. Further, having identified the presence and conductivity of the NVP-NZSP interface, it is clear that this is not the major contributor to the diphasic system resistance. It is not clear however, whether the conductive properties of this interface are intrinsic to the NVP-NZSP system (owing to similarities in chemistry/structure) or rather a benefit of the low temperature processing afforded by cold sintering. Future work would do well to explore the relationship between low temperature sintering conditions and the ionic/electronic conductivities across the so-formed interfaces. Furthermore, this work demonstrated that the co-sintered interface may be bounded by the conductivities of the constituent materials, so increasing the intrinsic conductivities of the pure materials may have beneficial effects on the interfacial conductivity. Indeed, this conclusion appears to be supported by the broader field, as evidenced by a recent review by Janek and Zeier[105], which echoes this paper in calling for high conductivity cathode materials, high conductivity interfaces, and processing which enables devices composed of such materials, for accelerating the development of solid-state batteries.

## 7. Conclusion

Ceramic matrix pellets of three diphasic systems were fabricated by cold sintering and subsequently characterized with impedance spectroscopy. The first two systems were composed of a ceramic active material (NVP) and conductive carbon (carbon black or carbon nanofibers), while the third system contained NVP and a solid-state sodium-ion electrolyte (NZSP). Cold sintering for all samples was applied at 375°C using sodium hydroxide as a transient solvent with a uniaxial pressure of 350 MPa and a three-hour dwell period. The resulting pellets were of high relative density ($\rho > 85\%$) and the microstructures exhibited microstructural hallmarks of sintering, despite the low sintering temperature and presence of additives. Only minor impurity phases were present in the cold sintered samples, in contrast to the complete loss of the primary phases when diphasic systems were heated in air above 600°C.

Cold sintered composites of carbon and NVP exhibited classical percolation behavior. In the case of carbon nanofibers, the percolation threshold was found to be around 3.8 vol.%, while the carbon black samples appeared to percolate near 2 vol.%. The lower percolation threshold for the carbon black samples was attributed to shearing at the grain boundaries of the ceramic as inferred from high resolution TEM observations. The electrical response near the percolation threshold for both diphasic systems exhibited interesting low frequency behavior, with the NVP grain boundary response gradually being replaced by electronic conduction and associated non-blocking behavior of the platinum electrodes. Beyond the percolation threshold, all samples exhibited electrical shorting through the carbon network within the composites.

For the cold sintered composites containing NVP and NZSP, we observed a progressive increase in conductivity as more solid electrolyte was added. As a function of volume percentage solid electrolyte, the total conductivity was characterized by a sharp increase in conductivity, followed by a relatively slow increase in conductivity from 20 to 80 vol.% solid electrolyte, followed by a sharp increase in conductivity towards the value of the pure solid electrolyte. An interfacial contribution to the resistance of the samples was identified and characterized, yielding insight into the properties and measurement of such interfaces for future solid-state battery research. The trend in total conductivity of the diphasic system suggests that a battery comprised of such materials would necessitate operation at high temperatures (> 100°C).

These results collectively contribute to the development of a potential relationship between the intrinsic conductivities of model solid-state battery materials and the resultant bulk conductivity. Aided by low temperature processing, such a relationship may be crucial in the development of high energy density, high performance, solid-state batteries based on ceramic matrices.

## 8. Author Contributions

**Conceptualization**, Z.G, C.A.R; **Methodology**, Z.G., C.A.R, Z.F.; **Investigation**, Z.G. Z.F., J.F.; **Formal Analysis**, Z.G., Z.F., J.F.; **Supervision**, C.A.R; **Writing – original draft**, Z.G.; **Writing – review and editing**, Z.G., Z.F., J.F., C.A.R.; **Funding Acquisition**, C.A.R.; **Project Administration**, C.A.R.

## 9. Conflicts of Interest

The authors declare no competing financial interest.

## 10. Acknowledgements

The authors would like to acknowledge the financial support for this work provided by the Pacific Northwest National Laboratory, managed by the Battelle Corporation under contract No. DE-AC05-76RL01830, as well as the Air Force Office of Scientific Research (FA9550-19-1-0372). The authors would like to thank Dr. Xiaolin Li and Dr. David Reed of the Pacific Northwest National Laboratory for their technical insights. The authors would also like to thank Professor Rajagopalan for his technical insight. The authors would also like to thank the Materials

Characterization Laboratory of the Materials Research Institute at the Pennsylvania State University for aiding in the collection of the data, especially Dr. Trevor Clark, Steven Perini, Jeff Long, Mike Norell, and Dr. Jennifer Gray. The authors would also like to thank the anonymous referees, whose insights during the review process certainly improved the clarity of the conclusions for the readers.

## 11. References

(1) Janek, J.; Zeier, W. G. A Solid Future for Battery Development. *Nature Energy*. 2016. https://doi.org/10.1038/nenergy.2016.141.

(2) Liu, T.; Zhang, Y.; Jiang, Z.; Zeng, X.; Ji, J.; Li, Z.; Gao, X.; Sun, M.; Lin, Z.; Ling, M.; Zheng, J.; Liang, C. Exploring Competitive Features of Stationary Sodium Ion Batteries for Electrochemical Energy Storage. *Energy Environ Sci* **2019**, *12* (5), 1512–1533. https://doi.org/10.1039/c8ee03727b.

(3) Vaalma, C.; Buchholz, D.; Weil, M.; Passerini, S. A Cost and Resource Analysis of Sodium-Ion Batteries. *Nat Rev Mater* **2018**, *3*, 1–11. https://doi.org/10.1038/natrevmats.2018.13.

(4) Randau, S.; Weber, D. A.; Kötz, O.; Koerver, R.; Braun, P.; Weber, A.; Ivers-Tiffée, E.; Adermann, T.; Kulisch, J.; Zeier, W. G.; Richter, F. H.; Janek, J. Benchmarking the Performance of All-Solid-State Lithium Batteries. *Nat Energy* **2020**, *5* (3), 259–270. https://doi.org/10.1038/s41560-020-0565-1.

(5) Seok, J.; Hyun, J.-H.; Jin, A.; Um, J. H.; Abruña, H. D.; Yu, S.-H. Visualization of Sodium Metal Anodes via Operando X-Ray and Optical Microscopy: Controlling the Morphological Evolution of Sodium Metal Plating . *ACS Appl Mater Interfaces* **2022**. https://doi.org/10.1021/acsami.1c24673.

(6) Kim, K. J.; Rupp, J. L. M. All Ceramic Cathode Composite Design and Manufacturing towards Low Interfacial Resistance for Garnet-Based Solid-State Lithium Batteries. *Energy Environ Sci* **2020**, *13* (12), 4930–4945. https://doi.org/10.1039/d0ee02062a.

(7) Balaish, M.; Kim, K. J.; Wadaguchi, M.; Kong, L.; Rupp, J. L. M. Interfaces in Oxide-Based Li Metal Batteries; 2022. https://doi.org/10.1002/aenm.202002689.

(8) Balaish, M.; Gonzalez-Rosillo, J. C.; Kim, K. J.; Zhu, Y.; Hood, Z. D.; Rupp, J. L. M. Processing Thin but Robust Electrolytes for Solid-State Batteries. *Nat Energy* **2021**, *6* (3), 227–239. https://doi.org/10.1038/s41560-020-00759-5.

(9) Uhlenbruck, S.; Dornseiffer, J.; Lobe, S.; Dellen, C.; Tsai, C. L.; Gotzen, B.; Sebold, D.; Finsterbusch, M.; Guillon, O. Cathode-Electrolyte Material Interactions during Manufacturing of Inorganic Solid-State Lithium Batteries. *J Electroceram* **2017**, *38* (2–4), 197–206. https://doi.org/10.1007/s10832-016-0062-x.

(10) Knauth, P. Ionic Conductor Composites: Theory and Materials. *J Electroceram* **2000**, *5* (2), 111–125. https://doi.org/10.1023/A:1009906101421.

(11) Hood, Z. D.; Zhu, Y.; Miara, L. J.; Chang, W. S.; Simons, P.; Rupp, J. L. M. A Sinter-Free Future for Solid-State Battery Designs. *Energy Environ Sci* **2022**, *15* (7), 2927–2936. https://doi.org/10.1039/d2ee00279e.

(12) Huang, K. J.; Ceder, G.; Olivetti, E. A. Manufacturing Scalability Implications of Materials Choice in Inorganic Solid-State Batteries. *Joule*. Cell Press March 17, 2021, pp 564–580. https://doi.org/10.1016/j.joule.2020.12.001.

(13) Miara, L.; Windmüller, A.; Tsai, C. L.; Richards, W. D.; Ma, Q.; Uhlenbruck, S.; Guillon, O.; Ceder, G. About the Compatibility between High Voltage Spinel Cathode Materials and Solid Oxide Electrolytes as a Function of Temperature. *ACS Appl Mater Interfaces* **2016**, *8* (40), 26842–26850. https://doi.org/10.1021/acsami.6b09059.

(14) Valiyaveettil-SobhanRaj, S.; Enterría, M.; Cid, R.; Saurel, D.; Nolis, G. M.; Marchini, F.; Thompson, T.; Aguesse, F.; Casas-Cabanas, M. Choosing Carbon Conductive Additives for NMC-LATP Composite Cathodes: Impact on Thermal Stability. *J Electrochem Soc* **2023**, *170* (4), 040523. https://doi.org/10.1149/1945-7111/ACCAB1.

(15) Boaretto, N.; Garbayo, I.; Valiyaveettil-SobhanRaj, S.; Quintela, A.; Li, C.; Casas-Cabanas, M.; Aguesse, F. Lithium Solid-State Batteries: State-of-the-Art and Challenges for Materials, Interfaces and Processing. *J Power Sources* **2021**, 229919. https://doi.org/10.1016/J.JPOWSOUR.2021.229919.

(16) Ichihara, F.; Miyoshi, S.; Masuda, T. Co-Sintering Process of LiCoO2 Cathodes and NASICON-Type LATP Solid Electrolytes Studied by X-Ray Diffraction and X-Ray Absorption Near Edge Structure. *Physical Chemistry Chemical Physics* **2022**. https://doi.org/10.1039/D2CP01020H.

(17) Agrawal, R. C.; Gupta, R. K. Superionic Solids: Composite Electrolyte Phase - an Overview. *J Mater Sci* **1999**, *34* (6), 1131–1162. https://doi.org/10.1023/A:1004598902146.

(18) Wei, L.; Liu, S.; Balaish, M.; Li, Z.; Zhou, X.; Rupp, J. L. M.; Guo, X. Customizable Solid-State Batteries toward Shape-Conformal and Structural Power Supplies. *Materials Today* **2022**, *xxx* (xx). https://doi.org/10.1016/j.mattod.2022.06.007.

(19) Su, Y.; Zhang, X.; Du, C.; Luo, Y.; Chen, J.; Yan, J.; Zhu, D.; Geng, L.; Liu, S.; Zhao, J.; Li, Y.; Rong, Z.; Huang, Q.; Zhang, L.; Tang, Y.; Huang, J. An All-Solid-State Battery Based on Sulfide and PEO Composite Electrolyte. *Small* **2022**, *18* (29), 1–12. https://doi.org/10.1002/smll.202202069.

(20) Tang, B.; Zhao, Y.; Wang, Z.; Chen, S.; Wu, Y.; Tseng, Y.; Li, L.; Guo, Y.; Zhou, Z.; Bo, S.-H. Ultrathin Salt-Free Polymer-in-Ceramic Electrolyte for Solid-State Sodium Batteries. *eScience* **2021**. https://doi.org/10.1016/j.esci.2021.12.001.

(21) Fan, L. Z.; He, H.; Nan, C. W. Tailoring Inorganic–Polymer Composites for the Mass Production of Solid-State Batteries. *Nat Rev Mater* **2021**, *0123456789*. https://doi.org/10.1038/s41578-021-00320-0.

(22) Evans, J.; Vincent, C. A.; Bruce, P. G. Electrochemical Measurement of Transference Numbers in Polymer Electrolytes. *Polymer (Guildf)* **1987**, *28* (13), 2324–2328. https://doi.org/10.1016/0032-3861(87)90394-6.

(23) Shao, Y.; Gudla, H.; Brandell, D.; Zhang, C. Transference Number in Polymer Electrolytes: Mind the Reference-Frame Gap. *J Am Chem Soc* **2022**. https://doi.org/10.1021/jacs.2c02389.

(24) Kudu, Ö. U.; Famprikis, T.; Fleutot, B.; Braida, M. D.; Le Mercier, T.; Islam, M. S.; Masquelier, C. A Review of Structural Properties and Synthesis Methods of Solid Electrolyte Materials in the Li2S − P2S5 Binary System. *J Power Sources* **2018**, *407* (July), 31–43. https://doi.org/10.1016/j.jpowsour.2018.10.037.

(25) Malugani, J. P.; Robert, G. Conductivite Ionique Dans Les Verres LiPO3LiX (X = I, Br, Cl). *Mater Res Bull* **1979**, *14* (8), 1075–1081. https://doi.org/10.1016/0025-5408(79)90075-8.

(26) Wang, C.; Liang, J.; Kim, J. T.; Sun, X. Prospects of Halide-Based All-Solid-State Batteries : From Material Design to Practical Application. *Sci Adv* **2022**, *9516* (September), 1–14. https://doi.org/eadc9516.

(27) Yersak, T.; Salvador, J. R.; Schmidt, R. D.; Cai, M. Hot Pressed, Fiber-Reinforced (Li 2 S) 70 (P 2 S 5 ). *ACS Appl Energy Mater* **2019**, *2*, 3523–3531. https://doi.org/10.1021/acsaem.9b00290.

(28) Giraldo, S.; Nakagawa, K.; Vásquez, F. A.; Fujii, Y.; Wang, Y.; Miura, A.; Calderón, J. A.; Rosero-Navarro, N. C.; Tadanaga, K. Preparation of Composite Electrodes for All-Solid-State Batteries Based on Sulfide Electrolytes: An Electrochemical Point of View. *Batteries* **2021**, *7* (4). https://doi.org/10.3390/batteries7040077.

(29) Sakuda, A.; Kuratani, K.; Yamamoto, M.; Takahashi, M.; Takeuchi, T.; Kobayashi, H. All-Solid-State Battery Electrode Sheets Prepared by a Slurry Coating Process. *J Electrochem Soc* **2017**, *164* (12), A2474–A2478. https://doi.org/10.1149/2.0951712jes.

(30) Yamamoto, M.; Takahashi, M.; Terauchi, Y.; Kobayashi, Y.; Ikeda, S.; Sakuda, A. Fabrication of Composite Positive Electrode Sheet with High Active Material Content and Effect of Fabrication Pressure for All-Solid-State Battery. *Journal of the Ceramic Society of Japan* **2017**, *125* (5), 391–395. https://doi.org/10.2109/jcersj2.16321.

(31) Otani, K.; Muta, T.; Furuta, T.; Miyuki, T.; Kaburagi, T.; Inoue, G. Ionic Conductivity Prediction Model for Composite Electrodes and Quantification of Ionic Conductivity Reduction Factors in Sulfide-Based All-Solid-State Batteries. *J Energy Storage* **2023**, *58* (December 2022), 106279. https://doi.org/10.1016/j.est.2022.106279.

(32) Tron, A.; Hamid, R.; Zhang, N.; Beutl, A. Rational Optimization of Cathode Composites for Sulfide-Based All-Solid-State Batteries. *Nanomaterials* **2023**, *13* (2). https://doi.org/10.3390/nano13020327.

(33) Busche, M. R.; Weber, D. A.; Schneider, Y.; Dietrich, C.; Wenzel, S.; Leichtweiss, T.; Schröder, D.; Zhang, W.; Weigand, H.; Walter, D.; Sedlmaier, S. J.; Houtarde, D.; Nazar, L. F.; Janek, J. *In Situ* Monitoring of Fast Li-Ion Conductor Li $_7$ P $_3$ S $_{11}$ Crystallization Inside a Hot-Press Setup. *Chemistry of Materials* **2016**, *28* (17), 6152–6165. https://doi.org/10.1021/acs.chemmater.6b02163.

(34) Grady, Z. A.; Wilkinson, C. J.; Randall, C. A.; Mauro, J. C. Emerging Role of Non-Crystalline Electrolytes in Solid-State Battery Research. *Frontiers in Energy Research*. Frontiers Media S.A. September 9, 2020, p 218. https://doi.org/10.3389/fenrg.2020.00218.

(35) Kravchyk, K. V.; Kovalenko, M. V. Perspective on Design and Technical Challenges of Li-Garnet Solid-State Batteries. *Sci Technol Adv Mater* **2021**, *0* (0). https://doi.org/10.1080/14686996.2021.2018919.

(36) Kravchyk, K. V; Zhang, H.; Okur, F.; Kovalenko, M. V. Li − Garnet Solid-State Batteries with LLZO Scaffolds. *Acc Mater Res* **2022**. https://doi.org/10.1021/accountsmr.2c00004.

(37) Buannic, L.; Naviroj, M.; Miller, S. M.; Zagorski, J.; Faber, K. T.; Llordés, A. Dense Freeze-Cast Li7La3Zr2O12 Solid Electrolytes with Oriented Open Porosity and Contiguous Ceramic Scaffold. *Journal of the American Ceramic Society* **2019**, *102* (3), 1021–1029. https://doi.org/10.1111/jace.15938.

(38) Wang, R.; Dong, Q.; Wang, C.; Hong, M.; Gao, J.; Xie, H.; Guo, M.; Ping, W.; Wang, X.; He, S.; Luo, J.; Hu, L. High-Temperature Ultrafast Sintering : Exploiting a New Kinetic Region to Fabricate Porous Solid-State Electrolyte Scaffolds. *Adv Energy Mater* **2021**, *2100726*, 1–8. https://doi.org/10.1002/adma.202100726.

(39) Huang, G.; Zhong, Y.; Xia, X.; Wang, X.; Gu, C.; Tu, J. Surface-Modified and Sulfide Electrolyte-Infiltrated LiNi0.6Co0.2Mn0.2O2 Cathode for All-Solid-State Lithium Batteries. *J Colloid Interface Sci* **2022**. https://doi.org/10.1016/j.jcis.2022.11.048.

(40) Xiao, Y.; Turcheniuk, K.; Narla, A.; Song, A. Y.; Ren, X.; Magasinski, A.; Jain, A.; Huang, S.; Lee, H.; Yushin, G. Electrolyte Melt Infiltration for Scalable Manufacturing of Inorganic All-Solid-State Lithium-Ion Batteries. *Nat Mater* **2021**, *20* (7), 984–990. https://doi.org/10.1038/s41563-021-00943-2.

(41) Ihrig, M.; Ye, R.; Laptev, A. M.; Grüner, D.; Guerdelli, R.; Scheld, W. S.; Finsterbusch, M.; Wiemhöfer, H.-D. D.; Fattakhova-Rohlfing, D.; Guillon, O. Polymer-Ceramic Composite Cathode with Enhanced Storage Capacity Manufactured by Field-Assisted Sintering and Infiltration. *ACS Appl Energy Mater* **2021**, *4* (10), 10428–10432. https://doi.org/10.1021/acsaem.1c02667.

(42) Nikodimos, Y.; Su, W.-N.; Taklu, B. W.; Merso, S. K.; Hagos, T. M.; Huang, C.-J.; Redda, H. G.; Wang, C.-H.; Wu, S.-H.; Yang, C.-C.; Hwang, B. J. Resolving Anodic and

Cathodic Interface-Incompatibility in Solid-State Lithium Metal Battery via Interface Infiltration of Designed Liquid Electrolytes. *J Power Sources* **2022**, *535* (January), 231425. https://doi.org/10.1016/j.jpowsour.2022.231425.

(43) Yu, T. H.; Huang, C. Y.; Wu, M. C.; Chen, Y. J.; Lan, T.; Tsai, C. L.; Chang, J. K.; Eichel, R. A.; Wu, W. W. Atomic-Scale Investigation of Na3V2(PO4)3 Formation Process in Chemical Infiltration via in Situ Transmission Electron Microscope for Solid-State Sodium Batteries. *Nano Energy* **2021**, *87* (April), 106144. https://doi.org/10.1016/j.nanoen.2021.106144.

(44) Han, F.; Gao, T.; Zhu, Y.; Gaskell, K. J.; Wang, C. A Battery Made from a Single Material. *Advanced Materials* **2015**, *27* (23), 3473–3483. https://doi.org/10.1002/adma.201500180.

(45) Kim, P.; Suu, K.; Hashiguchi, S.; Mikashima, T.; Oginosawa, T.; Iteue, W. Manufacturing Method for LiCoO2 Sintered Body and Sputtering Target, 2012. https://patentimages.storage.googleapis.com/3c/5d/6d/5ace4c244cea76/US20120305391A1.pdf (accessed 2018-09-11).

(46) Hamon, Y.; Douard, A.; Sabary, F.; Marcel, C.; Vinatier, P.; Pecquenard, B.; Levasseur, A. Influence of Sputtering Conditions on Ionic Conductivity of LiPON Thin Films. *Solid State Ion* **2006**, *177* (3–4), 257–261. https://doi.org/10.1016/j.ssi.2005.10.021.

(47) Nimisha, C. S.; Rao, K. Y.; Venkatesh, G.; Rao, G. M.; Munichandraiah, N. Sputter Deposited LiPON Thin Films from Powder Target as Electrolyte for Thin Film Battery Applications. *Thin Solid Films* **2011**, *519* (10), 3401–3406. https://doi.org/10.1016/j.tsf.2011.01.087.

(48) Julien, C. M.; Mauger, A.; Hussain, O. M. Sputtered LiCoO2 Cathode Materials for All-Solid-State Thin-Film Lithium Microbatteries. *Materials* **2019**, *12* (7), 1–26. https://doi.org/10.3390/ma12172687.

(49) Navone, C.; Tintignac, S.; Pereira-Ramos, J. P.; Baddour-Hadjean, R.; Salot, R. Electrochemical Behaviour of Sputtered C-V2O5 and LiCoO2 Thin Films for Solid State Lithium Microbatteries. In *Solid State Ionics*; 2011; Vol. 192, pp 343–346. https://doi.org/10.1016/j.ssi.2010.04.023.

(50) Tintignac, S.; Baddour-Hadjean, R.; Pereira-Ramos, J. P.; Salot, R. High Rate Bias Sputtered LiCoO2 Thin Films as Positive Electrode for All-Solid-State Lithium Microbatteries. *Electrochim Acta* **2014**, *146*, 472–476. https://doi.org/10.1016/j.electacta.2014.09.084.

(51) Yoon, Y.; Park, C.; Kim, J.; Shin, D. Characterization of Lithium Borophosphate Glass Thin Film Electrolytes Deposited by RF-Magnetron Sputtering for Micro-Batteries. In *Solid State Ionics*; 2012; Vol. 225, pp 636–640. https://doi.org/10.1016/j.ssi.2012.05.008.

(52) Xiao, D. L.; Tong, J.; Feng, Y.; Zhong, G. H.; Li, W. J.; Yang, C. L. Improved Performance of All-Solid-State Lithium Batteries Using LiPON Electrolyte Prepared with

Li-Rich Sputtering Target. *Solid State Ion* **2018**, *324* (July), 202–206. https://doi.org/10.1016/j.ssi.2018.07.011.

(53) Ferrari, V. C.; Kim, N. S.; Lee, S. B.; Rubloff, G. W.; Stewart, D. M. Co-Sputtering of Lithium Vanadium Oxide Thin Films with Variable Lithium Content to Enable Advanced Solid-State Batteries. *J Mater Chem A Mater* **2022**, 12518–12531. https://doi.org/10.1039/d2ta01021f.

(54) Valle, J. M.; Huang, C.; Tatke, D.; Wolfenstine, J.; Go, W.; Kim, Y.; Sakamoto, J. Characterization of Hot-Pressed von Alpen Type NASICON Ceramic Electrolytes. *Solid State Ion* **2021**, *369* (January), 115712. https://doi.org/10.1016/j.ssi.2021.115712.

(55) Luo, J.; Zhong, S.; Huang, Z.; Huang, B.; Wang, C. A. High Li+-Conductive Perovskite Li3/8Sr7/16Ta3/4Zr1/4O3 Electrolyte Prepared by Hot-Pressing for All-Solid-State Li-Ion Batteries. *Solid State Ion* **2019**, *338*, 1–4. https://doi.org/10.1016/j.ssi.2019.04.010.

(56) Patra, S.; Krupa B R, V.; Chakravarty, S.; Murugan, R. Microstructural Engineering in Lithium Garnets by Hot Isostatic Press to Cordon Lithium Dendrite Growth and Negate Interfacial Resistance for All Solid State Battery Applications. *Electrochim Acta* **2019**, *312*, 320–328. https://doi.org/10.1016/j.electacta.2019.05.003.

(57) Yersak, T. A.; Hao, F.; Kang, C.; Salvador, J. R.; Zhang, Q.; Malabet, H. J. G.; Cai, M. Consolidation of Composite Cathodes with NCM and Sulfide Solid-State Electrolytes by Hot Pressing for All-Solid-State Li Metal Batteries. *Journal of Solid State Electrochemistry* **2022**, No. 0123456789. https://doi.org/10.1007/s10008-021-05104-8.

(58) Laptev, A. M.; Zheng, H.; Bram, M.; Finsterbusch, M.; Guillon, O. High-Pressure Field Assisted Sintering of Half-Cell for All-Solid-State Battery. *Mater Lett* **2019**, *247*, 155–158. https://doi.org/10.1016/j.matlet.2019.03.109.

(59) Ihrig, M.; Mishra, T. P.; Scheld, W. S.; Häuschen, G.; Rheinheimer, W.; Bram, M.; Finsterbusch, M.; Guillon, O. Li7La3Zr2O12 Solid Electrolyte Sintered by the Ultrafast High-Temperature Method. *J Eur Ceram Soc* **2021**, *41* (12), 6075–6079. https://doi.org/10.1016/j.jeurceramsoc.2021.05.041.

(60) Ihrig, M.; Finsterbusch, M.; Tsai, C. L.; Laptev, A. M.; Tu, C. hao; Bram, M.; Sohn, Y. J.; Ye, R.; Sevinc, S.; Lin, S. kang; Fattakhova-Rohlfing, D.; Guillon, O. Low Temperature Sintering of Fully Inorganic All-Solid-State Batteries – Impact of Interfaces on Full Cell Performance. *J Power Sources* **2021**, *482*, 228905. https://doi.org/10.1016/j.jpowsour.2020.228905.

(61) Lalère, F.; Leriche, J. B.; Courty, M.; Boulineau, S.; Viallet, V.; Masquelier, C.; Seznec, V. An All-Solid State NASICON Sodium Battery Operating at 200 °C. *J Power Sources* **2014**, *247*, 975–980. https://doi.org/10.1016/J.JPOWSOUR.2013.09.051.

(62) Noi, K.; Suzuki, K.; Tanibata, N.; Hayashi, A.; Tatsumisago, M. Liquid-Phase Sintering of Highly Na+ Ion Conducting Na3Zr2Si2PO12 Ceramics Using Na3BO3 Additive.

*Journal of the American Ceramic Society* **2018**, *101* (3), 1255–1265. https://doi.org/10.1111/jace.15288.

(63) Leng, H.; Nie, J.; Luo, J. Combining Cold Sintering and Bi2O3-Activated Liquid-Phase Sintering to Fabricate High-Conductivity Mg-Doped NASICON at Reduced Temperatures. *Journal of Materiomics* **2019**, *5* (2), 237–246. https://doi.org/10.1016/j.jmat.2019.02.005.

(64) Srisurat, K.; Niyompan, A.; Tipakontitikul, R. Ionic Conductivity of β"-Alumina Solid Electrolyte Prepared by Liquid Phase Sintering Method. **2010**. https://doi.org/10.4028/www.scientific.net/AMR.93-94.513.

(65) Oh, J. A. S.; He, L.; Plewa, A.; Morita, M.; Zhao, Y.; Sakamoto, T.; Song, X.; Zhai, W.; Zeng, K.; Lu, L. Composite NASICON (Na3Zr2Si2PO12) Solid-State Electrolyte with Enhanced Na+ Ionic Conductivity: Effect of Liquid Phase Sintering. *ACS Appl Mater Interfaces* **2019**, *11* (43), 40125–40133. https://doi.org/10.1021/acsami.9b14986.

(66) Grady, Z. A.; Ndayishimiye, A.; Randall, C. A. A Dramatic Reduction in the Sintering Temperature of the Refractory Sodium β’’-Alumina Solid Electrolyte via Cold Sintering. *J Mater Chem A Mater* **2021**. https://doi.org/10.1039/d1ta05933e.

(67) Grady, Z.; Fan, Z.; Ndayishimiye, A.; Randall, C. A. Design and Sintering of All-Solid-State Composite Cathodes with Tunable Mixed Conduction Properties via the Cold Sintering Process. *ACS Appl Mater Interfaces* **2021**, *13* (40), 48071–48087. https://doi.org/10.1021/acsami.1c13913.

(68) Grady, Z. M.; Tsuji, K.; Ndayishimiye, A.; Hwan-Seo, J.; Randall, C. A. Densification of a Solid-State NASICON Sodium-Ion Electrolyte Below 400 °C by Cold Sintering With a Fused Hydroxide Solvent. *ACS Appl Energy Mater* **2020**, *3* (5), 4356–4366. https://doi.org/10.1021/acsaem.0c00047.

(69) Grady, Z.; Seo, J. H.; Tsuji, K.; Ndayishimiye, A.; Lowum, S.; Dursun, S.; Maria, J. P.; Randall, C. A. Cold Sintering for High-Temperature Electrochemical Applications. *Electrochemical Society Interface* **2020**, *29* (4), 59–65. https://doi.org/10.1149/2.F08204IF.

(70) Ndayishimiye, A.; Hwi, S.; Spiers, C. J.; Randall, C. A. Reassessing Cold Sintering in the Framework of Pressure Solution Theory. *J Eur Ceram Soc* **2022**, No. September. https://doi.org/10.1016/j.jeurceramsoc.2022.09.053.

(71) Guo, J.; Floyd, R.; Lowum, S.; Maria, J. P.; Herisson De Beauvoir, T.; Seo, J.-H.; Randall, C. A.; Beauvoir, T. H. De; Seo, J.-H.; Randall, C. A. Cold Sintering: Progress, Challenges, and Future Opportunities. *Annu Rev Mater Res* **2019**, *49* (1), 1–21. https://doi.org/10.1146/annurev-matsci-070218- 010041.

(72) Seo, J.-H.; Fan, Z.; Nakaya, H.; Rajagopalan, R.; Gomez, E.; Iwasaki, M.; Randall, C. A. Cold Sintering, Enabling a Route to Co-Sinter an All-Solid-State Lithium-Ion Battery. *Jpn J Appl Phys* **2021**. https://doi.org/10.35848/1347-4065/abdd4c.

(73) Guo, J.; Guo, H.; Baker, A. L.; Lanagan, M. T.; Kupp, E. R.; Messing, G. L.; Randall, C. A. Cold Sintering: A Paradigm Shift for Processing and Integration of Ceramics. *Angewandte Chemie - International Edition* **2016**, *55* (38), 11457–11461. https://doi.org/10.1002/anie.201605443.

(74) Bang, S.; Ndayishimiye, A.; Randall, C. Mechanistic Approach to Identify Densification Kinetics and Mechanisms of Zinc Oxide Cold Sintering I. *Acta Mater* **2019**. https://doi.org/10.2139/ssrn.3428070.

(75) Goglio, G.; Ndayishimiye, A.; Largeteau, A.; Elissalde, C. View Point on Hydrothermal Sintering: Main Features, Today's Recent Advances and Tomorrow's Promises. *Scr Mater* **2019**. https://doi.org/hrome.

(76) Entwistle, J.; Ge, R.; Pardikar, K.; Smith, R.; Cumming, D. Carbon Binder Domain Networks and Electrical Conductivity in Lithium-Ion Battery Electrodes : A Critical Review. *Renewable and Sustainable Energy Reviews* **2022**, *166* (June), 112624. https://doi.org/10.1016/j.rser.2022.112624.

(77) Minnmann, P.; Quillmann, L.; Burkhardt, S.; Richter, F. H.; Janek, J. Quantifying the Impact of Charge Transport Bottlenecks in Composite Cathodes of All-Solid-State Batteries. *J Electrochem Soc* **2021**, *168* (040537). https://doi.org/10.1149/1945-7111/abf8d7.

(78) Ohno, S.; Rosenbach, C.; Dewald, G. F.; Janek, J.; Zeier, W. G. Linking Solid Electrolyte Degradation to Charge Carrier Transport in the Thiophosphate-Based Composite Cathode toward Solid-State Lithium-Sulfur Batteries. *Adv Funct Mater* **2021**. https://doi.org/10.1002/adfm.202010620.

(79) Zatovsky, I. V. NASICON-Type Na3V2(PO4)3. *Acta Crystallogr Sect E Struct Rep Online* **2010**, *66* (2), 0–5. https://doi.org/10.1107/S1600536810002801.

(80) Boilot, J. P.; Collin, G.; Colomban, P. H. *Relation Structure-Fast Ion Conduction in the NASICON Solid Solution*; 1988; Vol. 73. https://ac.els-cdn.com/0022459688900655/1-s2.0-0022459688900655-main.pdf?_tid=bbc3753e-f1ed-4686-a6ad-018d588a973e&acdnat=1552428091_1e292822c1ff680ab9cacce42dfe3ad7 (accessed 2019-03-11).

(81) Shpanchenko, R. V.; Dikarev, E. V.; Mironov, A. V.; Mudretsova, S. N.; Antipov, E. V. Structural Transformations in the Na4+xVO(PO4)2 Vanadylphosphates. *J Solid State Chem* **2006**, *179* (8), 2681–2689. https://doi.org/10.1016/j.jssc.2006.05.013.

(82) Panin, R. V.; Shpanchenko, R. V.; Mironov, A. V.; Velikodny, Y. A.; Antipov, E. V.; Hadermann, J.; Tarnopolsky, V. A.; Yaroslavtsev, A. B.; Kaul, E. E.; Geibel, C. Crystal Structure, Polymorphism, and Properties of the New Vanadyl Phosphate Na4VO(PO4)2. *Chemistry of Materials* **2004**, *16* (6), 1048–1055. https://doi.org/10.1021/cm0351543.

(83) Naqash, S.; Ma, Q.; Tietz, F.; Guillon, O. Na3Zr2(SiO4)2(PO4) Prepared by a Solution-Assisted Solid State Reaction. *Solid State Ion* **2017**, *302*, 83–91. https://doi.org/10.1016/j.ssi.2016.11.004.

(84) Pereira da Silva, J. G.; Bram, M.; Laptev, A. M.; Gonzalez-Julian, J.; Ma, Q.; Tietz, F.; Guillon, O. Sintering of a Sodium-Based NASICON Electrolyte: A Comparative Study between Cold, Field Assisted and Conventional Sintering Methods. *J Eur Ceram Soc* **2019**, *39* (8), 2697–2702. https://doi.org/10.1016/J.JEURCERAMSOC.2019.03.023.

(85) Novikova, S. A.; Larkovich, R. V.; Chekannikov, A. A.; Kulova, T. L.; Skundin, A. M.; Yaroslavtsev, A. B. Electrical Conductivity and Electrochemical Characteristics of Na 3 V 2 (PO 4 ) 3 -Based NASICON-Type Materials. *Inorganic Materials* **2018**, *54* (8), 794–804. https://doi.org/10.1134/S0020168518080149.

(86) Irvine, B. J. T. S.; Sinclair, D. C.; West, A. R. Electroceramics Characterisation by Impedance Sepctroscopy. *Advanced Materials* **1990**, *2* (3), 132–138.

(87) Huggins, R. A. Simple Method to Determine Electronic Conductivity and Ionic Components of the Conductors in Mixed a Review. *Ionics (Kiel)* **2002**, *8* (3–4), 300–313. https://doi.org/10.1007/BF02376083.

(88) Lasia, A. The Origin of the Constant Phase Element. *J Phys Chem Lett* **2022**, *13* (2), 580–589. https://doi.org/10.1021/acs.jpclett.1c03782.

(89) Cho, I.; Choi, J.; Kim, K.; Ryou, M. H.; Lee, Y. M. A Comparative Investigation of Carbon Black (Super-P) and Vapor-Grown Carbon Fibers (VGCFs) as Conductive Additives for Lithium-Ion Battery Cathodes. *RSC Adv* **2015**, *5* (115), 95073–95078. https://doi.org/10.1039/c5ra19056h.

(90) McLachlan, D. S.; Blaszkiewicz, M.; Newnham, R. E. Electrical Resistivity of Composites. *Journal of the American Ceramic Society* **1990**, *73* (8), 2187–2203. https://doi.org/10.1111/j.1151-2916.1990.tb07576.x.

(91) Kidner, N. J.; Homrighaus, Z. J.; Ingram, B. J.; Mason, T. O.; Garboczi, E. J. Impedance/Dielectric Spectroscopy of Electroceramics-Part 1: Evaluation of Composite Models for Polycrystalline Ceramics. *J Electroceram* **2005**, *14* (3), 283–291. https://doi.org/10.1007/s10832-005-0969-0.

(92) Gompf, B.; Dressel, M.; Berrier, A. Impedance Spectroscopy and Equivalent Circuits of Metal-Dielectric Composites around the Percolation Threshold. *Appl Phys Lett* **2018**, *113* (24), 243104. https://doi.org/10.1063/1.5081097.

(93) Carmona, F.; Barreau, F.; Delhaes, P.; Canet, R. An Experimental Model for Studying the Effect of Anisotropy on Percolative Conduction. *Journal de Physique Lettres* **1980**, No. 22, 531–533. https://doi.org/10.1051/jphyslet:019800041022053100ï.

(94) Xu, X.; Carr, C.; Chen, X.; Myers, B. D.; Huang, R.; Yuan, W.; Choi, S.; Yi, D.; Phatak, C.; Haile, S. M. Local Multimodal Electro-Chemical-Structural Characterization of

Solid-Electrolyte Grain Boundaries. *Adv Energy Mater* **2021**, *2003309*, 2003309. https://doi.org/10.1002/aenm.202003309.

(95) Robertson, C. G.; Hardman, N. J. Nature of Carbon Black Reinforcement of Rubber: Perspective on the Original Polymer Nanocomposite. *Polymers (Basel)* **2021**, *13* (4), 1–28. https://doi.org/10.3390/polym13040538.

(96) Kim, J.; Eom, M.; Noh, S.; Shin, D. Effect of Mixing Method on the Properties of Composite Cathodes for All-Solid-State Lithium Batteries Using Li2SeP2S5 Solid Electrolytes. *J Power Sources* **2013**, *244*, 476–481. https://doi.org/10.1016/j.jpowsour.2012.11.049.

(97) Chen, Z.; Dahn, J. R. Reducing Carbon in LiFePO[Sub 4]/C Composite Electrodes to Maximize Specific Energy, Volumetric Energy, and Tap Density. *J Electrochem Soc* **2002**, *149* (9), A1184. https://doi.org/10.1149/1.1498255.

(98) Li, S.; Dong, Y.; Xu, L.; Xu, X.; He, L.; Mai, L. Effect of Carbon Matrix Dimensions on the Electrochemical Properties of Na 3 V 2 (PO 4 ) 3 Nanograins for High-Performance Symmetric Sodium-Ion Batteries. *Advanced Materials* **2014**, *26* (21), 3545–3553. https://doi.org/10.1002/adma.201305522.

(99) Huang, H. bo; Luo, S. hua; Liu, C. ling; Yang, Y.; Zhai, Y. chun; Chang, L. jiao; Li, M. qi. Double-Carbon Coated Na3V2(PO4)3 as a Superior Cathode Material for Na-Ion Batteries. *Appl Surf Sci* **2019**, *487* (May), 1159–1166. https://doi.org/10.1016/j.apsusc.2019.05.224.

(100) Saravanan, K.; Mason, C. W.; Rudola, A.; Wong, K. H.; Balaya, P. The First Report on Excellent Cycling Stability and Superior Rate Capability of Na3V2(PO4)3 for Sodium Ion Batteries. *Adv Energy Mater* **2013**, *3* (4), 444–450. https://doi.org/10.1002/aenm.201200803.

(101) Dudney, N. J. Enhanced Ionic Conductivity in Composite Electrolytes. *Solid State Ion* **1988**, *28–30* (PART 2), 1065–1072. https://doi.org/10.1016/0167-2738(88)90332-3.

(102) Maier, J. Nanoionics: Ion Transport and Electrochemical Storage in Confined Systems. *Nat Mater* **2005**, *4* (November), 805–815.

(103) Abram, E. J.; Sinclair, D. C.; West, A. R. A Strategy for Analysis and Modelling of Impedance Spectroscopy Data of Electroceramics: Doped Lanthanum Gallate. *J Electroceram* **2003**, *10* (3), 165–177. https://doi.org/10.1023/B:JECR.0000011215.56084.87.

(104) Hankin, A.; Bedoya-Lora, F. E.; Alexander, J. C.; Regoutz, A.; Kelsall, G. H. Flat Band Potential Determination: Avoiding the Pitfalls. *J Mater Chem A Mater* **2019**, *7* (45), 26162–26176. https://doi.org/10.1039/c9ta09569a.

(105) Janek, J.; Zeier, W. G. Challenges in Speeding up Solid-State Battery Development. *Nature Energy*. Nature Research 2023. https://doi.org/10.1038/s41560-023-01208-9.